atmosphere

MDPI

Article

Global Atmospheric $\delta^{13}CH_4$ and CH_4 Trends for 2000–2020 from the Atmospheric Transport Model TM5 Using CH_4 from Carbon Tracker Europe–CH_4 Inversions

Vilma Mannisenaho [1,*], Aki Tsuruta [1], Leif Backman [1], Sander Houweling [2,3], Arjo Segers [4], Maarten Krol [5,6], Marielle Saunois [7], Benjamin Poulter [8], Zhen Zhang [9], Xin Lan [10], Edward J. Dlugokencky [10], Sylvia Michel [11], James W. C. White [12] and Tuula Aalto [1]

1 Finnish Meteorological Institute, FI-00101 Helsinki, Finland; aki.tsuruta@fmi.fi (A.T.); leif.backman@fmi.fi (L.B.); tuula.aalto@fmi.fi (T.A.)
2 SRON Netherlands Institute for Space Research, 2333 CA Leiden, The Netherlands; s.houweling@sron.nl
3 Department of Earth Sciences, Vrije Universiteit Amsterdam, 1081 HV Amsterdam, The Netherlands
4 Department of Climate, Air & Sustainability, Netherlands Organisation for Applied Scientific Research (TNO), 3508 TA Utrecht, The Netherlands; arjo.segers@tno.nl
5 Department of Environmental Sciences, Wageningen University & Research, Meteorology and Air Quality, 6700 AA Wageningen, The Netherlands; maarten.krol@wur.nl
6 Institute for Marine and Atmospheric Research Utrecht IMAU, Utrecht University, Str. Princetonplein 5, 3584 CC Utrecht, The Netherlands
7 Laboratoire des Sciences du Climat et de l'Environnement, MCF–Université de Versailles Saint-Quentin, CEA-Orme des Merisiers, 91191 Gif-sur-Yvette, France; marielle.saunois@lsce.ipsl.fr
8 NASA Goddard Space Flight Center, 8800 Greenbelt Rd., Greenbelt, MD 20771, USA; benjamin.poulter@nasa.gov
9 Earth System Science Interdisciplinary Center, University of Maryland, 5825 University Research Ct Suite 4001, College Park, MD 20740, USA; yuisheng@gmail.com
10 NOAA Global Monitoring Laboratory (GML), 325 Broadway, Boulder, CO 80305, USA; xin.lan@noaa.gov (X.L.); ed.dlugokencky@noaa.gov (E.J.D.)
11 Institute of Arctic and Alpine Research (INSTAAR), University of Colorado, Campus Box 450, Boulder, CO 80309, USA; sylvia.englund@colorado.edu
12 Department of Earth Marine and Environmental Sciences, University of North Carolina at Chapel Hill, Chapel Hill, NC 27514, USA; jwcwhite@unc.edu
* Correspondence: vilma.mannisenaho@fmi.fi

check for updates

Citation: Mannisenaho, V.; Tsuruta, A.; Backman, L.; Houweling, S.; Segers, A.; Krol, M.; Saunois, M.; Poulter, B.; Zhang, Z.; Lan, X.; et al. Global Atmospheric $\delta^{13}CH_4$ and CH_4 Trends for 2000–2020 from the Atmospheric Transport Model TM5 Using CH_4 from Carbon Tracker Europe—CH4 Inversions. *Atmosphere* **2023**, *14*, 1121. https://doi.org/10.3390/atmos14071121

Academic Editors: Ge Han and Miao Zhang

Received: 23 April 2023
Revised: 30 May 2023
Accepted: 4 July 2023
Published: 6 July 2023

Abstract: This study investigates atmospheric $\delta^{13}CH_4$ trends, as produced by a global atmospheric transport model using CH_4 inversions from CarbonTracker-Europe CH_4 for 2000–2020, and compares them to observations. The CH_4 inversions include the grouping of the emissions both by $\delta^{13}CH_4$ isotopic signatures and process type to investigate the effect, and to estimate the CH_4 magnitudes and model CH_4 and $\delta^{13}CH_4$ trends. In addition to inversion results, simulations of the global atmospheric transport model were performed with modified emissions. The estimated global CH_4 trends for oil and gas were found to increase more than coal compared to the priors from 2000–2006 to 2007–2020. Estimated trends for coal emissions at 30° N–60° N are less than 50% of those from priors. Estimated global CH_4 rice emissions trends are opposite to priors, with the largest contribution from the EQ to 60° N. The results of this study indicate that optimizing wetland emissions separately produces better agreement with the observed $\delta^{13}CH_4$ trend than optimizing all biogenic emissions simultaneously. This study recommends optimizing separately biogenic emissions with similar isotopic signature to wetland emissions. In addition, this study suggests that fossil-based emissions were overestimated by 9% after 2012 and biogenic emissions are underestimated by 8% in the inversion using EDGAR v6.0 as priors.

Keywords: methane; isotopes; atmospheric modelling

1. Introduction

Methane (CH_4) is a greenhouse gas emitted into the atmosphere by natural and anthropogenic processes. Emissions can also be categorized according to their formation processes into biogenic, pyrogenic, and thermogenic emissions [1]. Atmospheric CH_4 concentrations have more than doubled since pre-industrial times [1]. The atmospheric concentration of CH_4 is well known, unlike the magnitude and contribution of each CH_4 source [2,3]. Atmospheric records show that the concentration of CH_4 was almost stable during the early 2000s but started to increase again after 2006. At the same time, observations of $^{13}CH_4$ show a decrease, i.e., the atmosphere is becoming more depleted in the heavy isotope [4].

CH_4 has two stable carbon isotopes, and their isotopic signatures ($\delta^{13}C$; deviation of the ratio relative to a standard) depend on the processes producing CH_4 [5]. In general, emissions from biogenic processes are most depleted in ^{13}C, and emissions of pyrogenic origin are most enriched in ^{13}C, followed by thermogenic sources (e.g., [5,6]). At present, isotopic measurements are limited in both spatial and temporal coverage, while partly overlapping signatures make source attribution uncertain [7]. Furthermore, the isotopic signatures of emissions can vary from place to place due to differences in production processes, types of origin, or methanogenesis [8–11]. It is important to have detailed spatial information on isotopic signatures; otherwise, the results may be erroneous [8]. In combination with atmospheric inversions with only total CH_4 budgets (e.g., [1,12]), isotopic information is helpful in characterizing CH_4 sources [7,13–15]. In addition CH_4 emissions, all sinks have fractionation factors, and there are uncertainties such as the fractionation factor of OH, which also varies between studies [16,17]. There is also some uncertainty in the tropospheric Cl sink, which varies from 13–37 Tg CH_4 yr^{-1} [18] to 12–13 Tg CH_4 yr^{-1} [19] and even smaller estimates [20].

Previous studies have proposed a variety of causes for the CH_4 plateau in the early 2000s and the post-2006 growth. Lan et al. [15] concluded, using the forward modeling of atmospheric chemistry, that fossil fuel emissions are unlikely to be the dominant driver of global CH_4 growth after 2006 and that a significant reduction in OH would not correspond to the observed decrease in global mean $\delta^{13}CH_4$. Lassey and Ragnauth [21] also concluded that it is unlikely that the post-2006 increase is primarily due to sinks of OH and Cl. In addition, Thompson et al. [13], Zhang et al. [22] concluded that changes in the atmospheric sink are not significant to the recent increase in global CH_4. Similarly, Milkov et al. [23] found that emissions from shale gas and shale oil are not the dominant driver of the increase in global CH_4, even though emissions from these sources are expected to increase. Instead, Milkov et al. [23] proposed that changes in the emissions of isotopically lighter CH_4 dominate the increase in global CH_4. Yin et al. [24] used ensemble inverse modeling to suggest that the recent acceleration in the CH_4 growth rate from 2010 to 2017 is due to increases in CH_4 emissions, particularly from wetlands in the tropics and anthropogenic emissions from China, rather than variations in OH. Similarly, Zhang et al. [22] suggested that the high grow rates from 2016 to 2018 are due to increases in tropical and boreal wetlands with increased anthropogenic emission, especially livestock emissions in tropical regions.

A box-model analysis by Schaefer et al. [25] suggested that decreasing thermogenic emissions and/or changes in OH concentrations, which is an atmospheric sink for CH_4, are responsible for the plateau in the early 2000s. On the contrary, Fujita et al. [26] suggest that the plateau is explained by decreases in biogenic and biomass burning CH_4 emissions. In contrast, Zhang et al. [27] suggest that the decreased coal, oil, and gas emissions, together with the anomaly of increasing OH, contributed to the plateau. Schaefer et al. [25] suggests that the growth after 2006 is predominantly biogenic and more consistent with agriculture than wetlands, and tropical regions have shown the highest increase based on satellite measurements [12]. Thompson et al. [13], Fujita et al. [26] also suggest that biogenic emissions from the tropics are responsible for the growth after 2006. Zhang et al. [27] suggest that the post-2006 growth is primarily due to increases in agriculture and landfill and waste sectors with minor contributions from increased emissions from industrial fossil

and wetland. Bousquet et al. [28] found that Arctic warming increased emissions from wetlands in 2007. Dlugokencky et al. [29] estimated that tropical wetland CH_4 emissions increased during La Niña conditions in 2007 and 2008, contributing to the global increase in CH_4, as natural wetland CH_4 emissions in the tropics are driven by precipitation, which is enhanced during La Niña conditions in some regions. Lassey and Ragnauth [21] also suggest that southern tropical wetlands may be behind the increase in global CH_4 after 2006.

Previous CH_4 inversion studies divide emissions into anthropogenic, biospheric, and other categories (e.g., [30,31]). The category of anthropogenic emissions include all CH_4 emissions from human activity, while biospheric emissions include emissions from wetlands and soil sinks. The other emissions include geological, ocean, and termite emissions. In this study, we challenge the traditional division of emissions and instead group the emissions based on their isotopic signatures and origin. In this study, we categorize the emissions based on their isotopic signatures: fossil-based and more enriched in $^{13}CH_4$ and biogenic with depleted $^{13}CH_4$.

We performed two inversion runs using a CarbonTracker Europe –CH_4 data assimilation system using CH_4 mole fraction data. The TM5 atmospheric chemistry model was run using the posterior fluxes and process-specific isotopic signatures to examine atmospheric $\delta^{13}CH_4$ and CH_4 trends. Furthermore, the simulations were also performed with TM5, which included 1) increasing wetland emissions and 2–3) changing the ratio of biogenic to fossil emissions in the anthropogenic sources. The results from the study show the role of fossil emissions in the global methane budget and that grouping sources isotopically is an effective way to optimize emissions in atmospheric inversions.

2. Materials and Methods

2.1. CarbonTracker-Europe-CH_4

CarbonTracker-Europe-CH_4 (CTE-CH_4) is an atmospheric inversion model that optimizes surface CH_4 fluxes globally using the Ensemble Kalman Filter (EnKF) [32] as the model scheme [30,33]. The atmospheric chemistry transport model TM5 [34] (see Section 2.1.1) is used as an observation operator EnKF. TM5 uses a priori information on the CH_4 fluxes, the initial mole fraction of atmospheric CH_4, and ECMWF ERA5 meteorological reanalysis data to compute estimated atmospheric concentrations, after which the EnKF is applied to optimize emission fields for anthropogenic and biogenic sources using the observed atmospheric concentrations [30]. TM5 in the CTE-CH_4 is run at a global resolution of 4° × 6° (latitude × longitude) with a 1° × 1° zoom and 2° × 3° intermediate zoom surrounding the 1° × 1° zoom grid over Europe (see more details in Section 2.1.1).

CTE-CH_4 optimizes fluxes from two categories simultaneously at a weekly resolution. The horizontal resolution of the optimization varies: for northern land, including Canada, the USA, Europe, and Russia, fluxes are optimized grid-wise, and elsewhere, they are optimized region-wise (see, e.g., [35]). The two categories are assumed to be independent, with an uncertainty of 80% over land and 20% over oceans. The spatial correlation length varies from 100 to 900 km between optimized regions, depending on the grid or optimization region size and observation density (see Tenkanen et al. [35] for details). Uncertainties for emissions are calculated for each emission source based on its prior or posterior ratio of the category in the model.

2.1.1. TM5

TM5 is a global Eulerian atmospheric chemistry transport model [34]. It is driven by ECMWF ERA5 meteorological fields with a 1° × 1° (latitude × longitude) zoom grid over Europe (up to 74° N) embedded in a 4° × 6° global grid with an intermediate 2° × 3° zoom region (e.g., [30]). TM5 includes off-line chemical reactions with OH, Cl, and $O(^1D)$, where the the reaction with OH is the largest atmospheric sink of CH_4. The reaction with OH is calculated based on Houweling et al. [12], and the monthly variations in OH concentrations from Spivakovsky et al. [36] are scaled by 0.92 based on an evaluation with

methyl chloroform [37]. Atmospheric sinks of Cl and $O(^1D)$ are considered only in the stratosphere, where the reaction rates are prescribed based on the atmospheric chemistry general circulation model ECHAM5/MESSy1 [38]. The TM5 in this study does not consider any interannual variability in the photochemical sink processes, as they are assumed to be small during the study period [39–41].

In this study, TM5 in CTE-CH_4 includes only CH_4, but the forward runs based on the results of the inversions include both total CH_4 (incl. $^{12}CH_4$ and $^{13}CH_4$) and $^{13}CH_4$. The kinetic isotope effects (KIE) $k(^{12}CH_4)/k(^{13}CH_4)$ of 1.004 and 1.013 are used for $^{13}CH_4$ OH and $O(^1D)$, respectively [16], and 1.066 [42] is used for Cl. In this study, the TM5 forward model applied after the inversions assumes that the KIE of the total CH_4 is the same as for $^{12}CH_4$, i.e., $k(^{12}CH_4)/k(^{13}CH_4) \approx k(CH_4)/k(^{13}CH_4)$.

In this study, we also include the CH_4 sink to dry soils (i.e., a negative flux from the atmosphere to the soil) in the lowermost layer of TM5. The soil sink depends on soil moisture, temperature, and soil texture, resulting in the smallest sink in winter and the largest sink in the summer [43].

Soil sink removal rate of $^{13}CH_4$ is calculated as [44]

$$L_{\text{soil},13} = \frac{F_{\text{soil},12}}{h \cdot \text{KIE}_{\text{soil}}} \times \frac{[^{13}CH_4]}{[^{12}CH_4]} \quad (1)$$

where $F_{\text{soil},12}$ is the negative flux of $^{12}CH_4$ at the surface, h is the thickness of the lowermost layer, $[^{12}CH_4]$ and $[^{13}CH_4]$ are the atmospheric concentrations of $^{12}CH_4$ and $^{13}CH_4$, and KIE_{soil} is assumed to be 1.0177 [45].

In the TM5 forward simulations, we include two separate tracers, CH_4 (incl. $^{12}CH_4$ and $^{13}CH_4$) and $^{13}CH_4$. The $\delta^{13}CH_4$ ($\delta^{13}C$) is calculated as follows:

$$\delta^{13}CH_4 = \left(\frac{(^{13}C/^{12}C)_{\text{sample}}}{(^{13}C/^{12}C)_{\text{std}}} - 1 \right) \times 1000, \quad (2)$$

where $(^{13}C/^{12}C)_{\text{std}} = 0.0112372$ is the isotopic (^{13}C and ^{12}C) ratio of the standard, Vienna Pee-Dee Belemnite (VPDB; [46]).

2.2. CH_4 and $^{13}CH_4$ Fluxes

In this study, we use inventories and process-based model data for global CH_4 flux fields from anthropogenic and natural sources. All the CH_4 fields are pre-processed to a $1^\circ \times 1^\circ$ grid to match the TM5 model resolution. The $^{13}CH_4$ fluxes are obtained using Equation (2).

CH_4 anthropogenic flux data are taken from the EDGAR inventory v6.0 [47,48]. The data used in this study cover the years 2000–2020. The anthropogenic emissions include emissions from coal, oil and gas, residential, rice cultivation, landfills and wastewater treatment (LWW), and enteric fermentation and manure management (EFMM). EDGAR v6.0 includes the seasonal cycle of emissions.

Anthropogenic emissions can be of fossil or biogenic origin, and the grouping between them is based on the processes by which CH_4 is formed, using isotopic signatures. In general, fossil sources are more enriched in $^{13}CH_4$ than emissions of biogenic origin.

Emissions from wetlands, soil sinks, and termites are taken from Saunois et al. [1]. Wetland emissions are the climatological monthly means from the bottom-up models for 2000–2017. Biomass burning emissions are taken from the Global Fire Emissions Database (GFED) v4.1 [49], ocean emissions from Weber et al. [50], and geological emissions from Etiope et al. [10]. Based on the Intergovernmental Panel on Climate Change (IPCC) AR6 WG1 report [51], we scaled the geological emissions to obtain the total global emissions of 23 Tg.

2.3. Atmospheric Observations

Atmospheric observations for CH_4 were taken from the National Oceanic and Atmospheric Administration—Global Monitoring Laboratory (NOAA/GML) and other national

and international networks [52], and the observations of $\delta^{13}C$ were taken from the Institute of Arctic and Alpine Research (INSTAAR) and the University of Colorado Boulder [53]. We used the CH_4 observations from NOAA/GML and the $\delta^{13}C$ observations to evaluate the simulation results and trends. The uncertainty target for CH_4 is 3 ppb [54], and for $\delta^{13}C$, the reproducibility of the measurements is 0.08‰ ± 0.02‰ [55].

2.3.1. CH_4 Observations for Constraining CH_4 Fluxes

Atmospheric observations for CH_4 mole fractions were obtained from NOAA/GML and other national and international networks and assimilated in the CTE-CH_4. The CH_4 observations include surface observations from continuous and flask samples, i.e., weekly discrete air samples. The hourly data from the continuous in situ CH_4 observations were processed similarly to Tsuruta et al. [30] before the inversions were performed. Observation uncertainties were defined for each site and observation based on the site's characteristics and the measurement accuracy. The observation uncertainty is defined by taking into account both the observation error and the TM5 model error. The model error arises from the ability of the TM5 to simulate the observations. The observation uncertainty is somewhat arbitrary and based on expert judgement [3,30,56]. Observations were not assimilated to constrain posterior CH_4 fluxes if the absolute differences between observations and prior mole fractions were greater than three times the observation uncertainty.

2.3.2. $\delta^{13}CH_4$ Observations for Evaluation

We used observations of $\delta^{13}CH_4$ to evaluate the emission trends and model estimates. Anomalies in the trends were used for comparison. We used curve fitting methods from Thoning et al. [57] to calculate the trend. The trend curve represents the long-term trend with seasonal cycles removed. Anomalies were obtained by subtracting the mean of the time series. In this study, we compared the model with observations at 13 stations, which has a long enough data time series, as shown in Table 1 and Supplementary Table S1.

Table 1. List of stations.

Station	Station Code	Country	Latitude	Longitude	Elevation [m a.s.l.]	Intake Height [m a. g.]
Barrow	BRW	Alaska, USA	71.32° N	156.61° W	11.00	5–16.5
Mace Head	MHD	Ireland	53.33° N	9.9° W	5.00	21
Niwot Ridge	NWR	Colorado, USA	40.05° N	105.59° W	3526	3
South Pole	SPO	Antarctica	89.98° S	24.8° W	2821.3	3–11.3

2.4. Isotopic Signatures

Each CH_4 source was assigned to a process a specific isotopic signature (Table 2) in a same way as previously carried out by Kangasaho et al. [44], which was used together with Equation (2) to calculate the global $^{13}CH_4$ flux fields from CH_4 emission fields. For LWW, rice, residential, ocean, and termite emissions, a single isotopic value was used, and the signature was taken from Thompson et al. [13] (mean values). For the remaining categories (EFMM, coal, oil and gas, wetlands, biomass burning, and geological) a spatially varying isotopic signature was used from Feinberg et al. [9]. EFMM isotopic signatures consider the local ratio of C3 and C4 vegetation [58] and the emitted isotopic signatures of livestock fed with C3 or C4 diets [59]. Country-level natural gas and oil signatures [59] were used in the oil and gas isotopic signatures in Feinberg et al. [9]. The M-COAL version presented by Feinberg et al. [9] and references therein were used as coal isotopic signatures, which are based on coal rank and depth. Globally varying isotopic signatures for geological emissions were taken from Etiope et al. [10]. Wetland isotopic signatures were based on observations characterizing wetland ecosystems taken from Ganesan et al. [8].

The original resolution of the isotopic signatures from Feinberg et al. [9] was T42 resolution but were converted to 1° × 1° resolution by selecting the closest coordinate value and by simple grid-averaging, respectively, for [44]. For all sources, the grid cells,

where isotopic signature data were not available from the data described above, were filled with mean values from Thompson et al. [13] (see Table 2) according to Kangasaho et al. [44].

Table 2. Isotopic signatures used to convert CH_4 flux fields to $^{13}CH_4$ fields. For spatially varying global values, the ranges of values are shown. Please see Kangasaho et al. [44] for spatial distributions. Isotopic signatures from Monteil et al. [14] are also presented for comparison.

Emission Source	Signature Value (‰) (Used in This Study)	Signature Value (‰) [14]
Enteric Fermentation and Manure Management (EFMM)	[−67.9,−54.5] [1], −66.8 [2]	−62
Landfills and Waste Water Treatment (LWW)	−55.6 [2]	−55
Rice (RICE)	−62.1 [2]	−63
Coal	[−64.1, −36.1] [1], −40 [2]	−35
Oil and Gas	[−56.6, −29.1] [1], −40 [2]	−40
Residential	−40 [2]	−38
Wetlands	[−74.9, −50] [3], −61.3 [2]	−59
Fires	[−25, −12] [1], −22.2 [2]	−21.8
Ocean	−47 [2]	−59
Termites	−65.2 [2]	−57
Geological	[−68, −24.3] [4], −40 [2]	−40

[1] Feinberg et al. [9], [2] Thompson et al. [13], [3] Ganesan et al. [8], [4] Etiope et al. [10].

We acknowledge the differences in the spatial distributions of emissions used in, e.g., Feinberg et al. [9] against the EDGAR v6.0. We are also aware of the seasonal variations in $\delta^{13}CH_4$ signatures, but in this study, the seasonal variations in $\delta^{13}CH_4$ signatures are not taken into account. However, considering the wide range of source signatures [5–7,60], we assume that our values are reasonable for the purposes of this study.

2.5. Model Setup

We used different set-ups for the inversions, which are described in Section 2.5.1. The different model set-ups for the TM5 transport model are described in detail in Section 2.5.2.

2.5.1. Inversion Model—CH_4 Only

The inversions differ in the categorization of the optimized fluxes (Table 3). For each category, one flux-scaling factor is applied per optimized region (see Section 2.1). In ORIG, the optimized category 1 (categ1) includes all anthropogenic sources, i.e., coal, oil, and gas, EFMM, LWW , rice, and residential, as well as biomass burning. Category 2 (categ2) includes wetlands and soil sinks. This division was used in, e.g., Saunois et al. [1]. This kind of division does not consider the differences in isotopic signatures, and the CH_4 budgets can be better resolved when emissions with similar isotopic signatures are optimized in the same category. Therefore, we wanted to optimize emissions together with similar isotopic signatures, so SET1 and SET2 inversions were performed. In SET1, categ1 includes coal and oil and gas, and categ2 includes EFMM, LWW, rice, wetlands, and soil sinks. In SET2, categ1 includes coal and oil and gas, and categ2 includes EFMM, LWW, and rice. In all inversions, the emission sources that are not included in categ1 or categ2 are taken as priors and not optimized.

Table 3. Model setup.

Simulation	Optimised (categ1)	Optimised (categ2)	Not Optimised (categ3)
ORIG	coal oil and gas agriculture * residential fires	wetlands soil sink	geological termites ocean
SET1	coal oil and gas	agriculture * soil sink wetlands	residential fires geological termites ocean
SET2	coal oil and gas	agriculture *	residential fires geological termites ocean wetlands soil sink

* Agriculture emissions include emissions from rice cultivations, enteric fermentation and manure management (EFMM) and landfills and wastewater treatment (LWW).

2.5.2. TM5 Forward Model with $\delta^{13}CH_4$

We performed a spin-up including $\delta^{13}CH_4$ prior to the TM5 simulation for the years 2000–2020. For the spin-up, we ran TM5 40 times using year 2000 emissions and meteorological fields, together with the isotopic signatures described in Sections 2.2 and 2.4. The spin-up was performed to obtain a well-mixed initial field for the TM5 forward modeling. The spin-up is important because the inversion did not include $\delta^{13}CH_4$ but only CH_4.

We performed a total of nine simulations using TM5 (Table 4). Out of these nine, six simulations were performed using prior and posterior emissions from ORIG, SET1, and SET2 inversions. The prior simulations for ORIG and SET1 are the same, but SET2 differs from ORIG and SET1. For the prior simulations, the spin-up was performed with posterior fluxes, and the same initial fields were used for the simulations with the prior fluxes.

We also modified the emissions after 2012 for the ORIG simulation to examine the effect of the ratio of fossil to biogenic emissions and to obtain a stronger response of the isotopic trend to the emission change. We increased the ratio of biogenic (including emissions from rice, LWW, EFMM, and wetlands) to fossil (including emissions from coal, oil and gas, and residential) by 2% from 74% to 76%. The ratio is defined as follows: ((rice + LWW + EFMM) + wetland)/((rice + LWW + EFMM) + wetland+ (coal + oil and gas + residential)). This increase was achieved by increasing wetland emissions by 29% (43.3 Tg yr^{-1}) (WET); decreasing fossil emissions by 9%, and increasing rice, LWW, and EFMM emissions by 2% (COMBO_1). In addition, we changed the biogenic fossil ratio to be 77% by decreasing fossil emissions by 9% and increasing rice, LWW, and EFMM emissions by 8% (COMBO_2).

Table 4. Different TM5 simulations. Emission sources and modifications to emissions are shown.

Simulation	Emissions	Modifications
ORIG	ORIG posteriors	
ORIGpri	ORIG priors	
SET1	SET1 posteriors	
SET1pri	SET1 priors	
SET2	SET2 posteriors	
SET2pri	SET2 priors	

Table 4. *Cont.*

Simulation	Emissions	Modifications
WET	ORIG posteriors	After 2012: Wetland emissions +29%
COMBO_1	ORIG posteriors	After 2012: Oil and gas, coal and residential −9% EFMM, LWW and Rice +2%
COMBO_2	ORIG posteriors	After 2012: Oil and gas, coal and residential −9% EFMM, LWW and Rice +8%

3. Results

3.1. Estimated CH_4 Fluxes

The results for estimated CH_4 fluxes are divided into two sections. Section 3.1.1 focuses on differences in the CH_4 budget at 30 degree latitudinal bands and globally. Section 3.1.2 focuses on an analysis of the emission change during different time periods (2000–2006, 2007–2013, and 2014–2020), both globally and in 30-degree latitudinal bands.

3.1.1. Estimated Emission Budgets

The estimated global posterior CH_4 emissions for oil and gas are higher compared to priors after 2010 (Figure 1). SET1 and SET2 estimate higher posterior emissions for oil and gas compared to ORIG, on average 3.16–3.19 $TgCH_4$ yr^{-1} (Table S2), and this is statistically significant ($p < 0.05$). In general, the largest contribution to the increase in oil and gas emissions in the posteriors comes from latitudes EQ–60° N (Figures S3 and S4). In contrast, posterior global coal emissions do not increase as much as priors suggest after 2007 in any of the simulations (Figure 1). The most significant difference in the magnitude of posterior and prior coal emissions occurs at latitudes 30° N–60° N (Figure S4). On average, posterior coal emissions are 0.86–4.72 $TgCH_4$ yr^{-1} lower than priors, although the result is not statistically significant ($p > 0.05$) (Table S2). Residential posterior emissions in ORIG differ in magnitude and trend from SET1 and SET2 (Figure 1), with the largest contribution coming from latitudes EQ–60° N (Figures S3 and S4). However, on average, the total estimated residential emissions in ORIG are 0.13 Tg yr^{-1} (Table S2) lower than prior. Residential emissions in SET1 and SET2 are not optimized.

Global LWW- and EFMM-estimated CH_4 emissions have a similar trend to the priors, but the magnitudes are higher (Figure 1 and Table S2). Average prior LWW emissions are approx. 1.7–4.2 $TgCH_4$ yr^{-1} smaller than the posteriors, and EFMM posterior emissions are 7.8–9.8 $TgCH_4$ yr^{-1} larger than in the priors in all inversions (Table S2). The largest contribution to the increase in LWW and EFMM posterior emissions comes from latitudes 90° S–EQ and 30° N–60° N (Figures S2 and S4). The global posterior rice emissions show an opposite trend to the prior emissions. However, the global total differs, on average, by less than 1 $TgCH_4$ yr^{-1} (Table S2).

The global posterior wetland CH_4 emissions differ between the simulations (Figure 1). SET1 estimates the largest posterior wetland CH_4 emissions among the total simulations. The largest contribution to the increase in SET1 wetland emissions comes from latitudes 30° S–EQ and 30° N–60° N (Table S2).

The global average soil-sink posteriors vary among simulated years, and no clear trend is visible for the years 2000–2014 (Figure 1). However, a strong decrease in the soil sink is estimated by SET1 in 2018, along with an increase in ORIG (and SET2). Termite, ocean, and geological emissions are not optimized in any simulation; therefore, posterior and prior emissions are the same (Table S2). Residential and fire emissions were optimized in ORIG in the biomass burning but are not optimized in SET1 or SET2. However, the estimated fire emissions differ very little from priors.

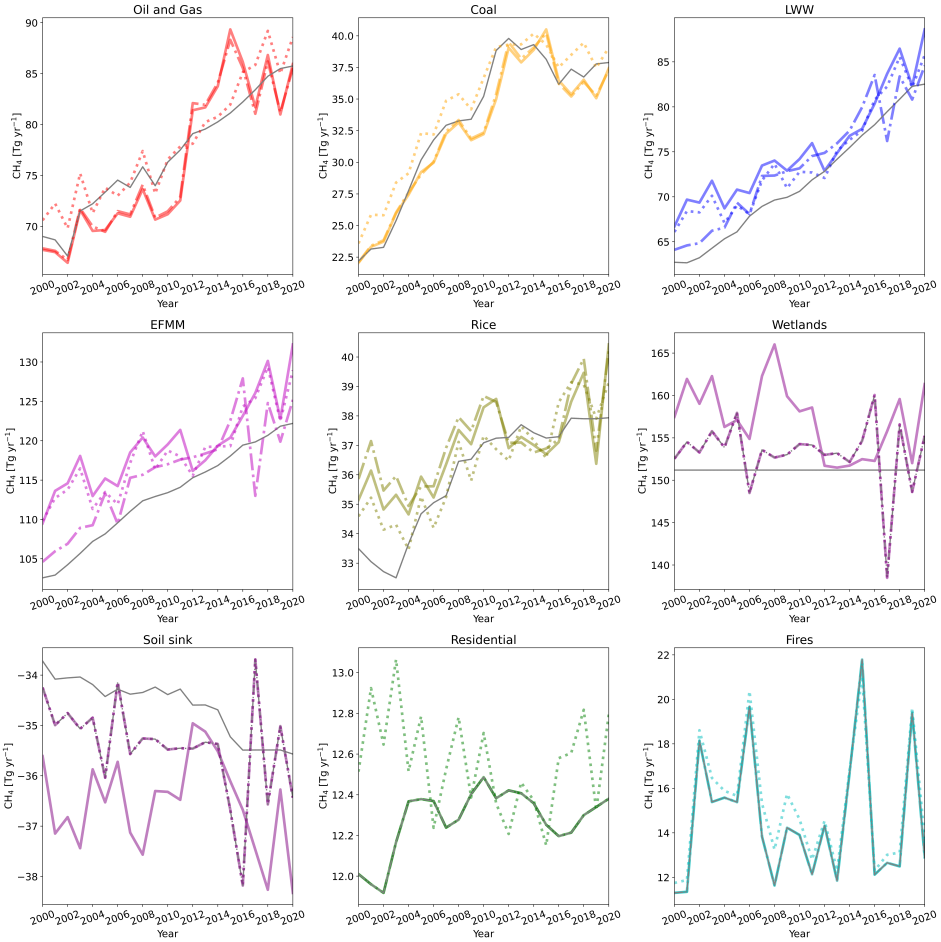

Figure 1. Global prior and posterior CH_4 emissions by sector. Solid lines are SET1, dash–dot lines are SET2, and dotted lines are ORIG. Posterior emission are bolded, and prior emissions are presented in gray. For emissions from residential and fires, please note that priors (SET1, SET2 and ORIG) are the same as posteriors for SET1 and SET2.

3.1.2. Emission Changes during 2000–2006, 2007–2013, and 2014–2020

Globally, oil and gas, EFMM, and LWW prior and posterior CH_4 emissions show an increasing trend (Figure 2). Coal emissions in SET1 and SET2 also show a globally increasing trend. The posterior mean LWW and coal emissions suggest a smaller increasing trend for CH_4 emissions compared to the priors (Figure 2). EFMM and oil and gas trends for SET1 and SET2 show a stronger increasing trend in comparison to the priors (Figure 2). However, the estimated EFMM trend from 2000–2006 to 2007–2013 is slightly smaller (<0.1 $TgCH_4\ yr^{-1}$) for SET1 (Figure 2 and Table S2). The contributions of different latitude bands to the global EFMM CH_4 posterior trend is different. At the latitudes 30° S–EQ, the EFMM posterior trend is decreased from 2007–2013 to 2014–2020 (Figure 3). At the latitudes 30° N–60° N, the posterior trends in SET1 and SET2 are opposite to the prior trends from 2000–2006 to 2007–2013. From 2007–2013 to 2014–2020, the trend increases again, similar to the priors, but the increasing trend in ORIG is 69% larger than that in the priors (Figure 4 and Table S3). At the latitudes 60° N–90° N, the posterior trend differs only a little from the priors, although the decrease in ORIG from 2000–2006 to 2013-2020 is more than twice as large as in the priors (Figures S6 and S7). At the latitudes 90° S–30° S, the EFMM posterior trends are stronger from 2000–2006 to 2007–2013 in all simulations but weaker from 2000–2006 to 2014–2020 for SET1 and SET2. LWW emissions have a globally increasing trend, but there are differences between the latitude bands and the simulations. The trend at 30° N–60° N and 90° S–30° S is opposite to that of the priors from 2000–2006 to 2007–2013 (Figures 4 and S6). The increasing trends for LWW emission in the posteriors

are smaller than in the priors, except for SET1 and SET2 for 90° S–EQ from 2000–2006 to 2014–2020 and also for 30° S–EQ from 2000–2006 to 2007–2013 (Figures 2, 3, 5 and S7). However, all simulations show a larger decreasing trend than priors at 60° N–90° N and 90° S–30° S from 2000–2006 to 2007–2013. The stronger decreasing trend from 2000–2006 to 2014–2020 continues at 60° N–90° N (Figures S6 and S7). Estimated posterior trends for oil and gas emissions at 60° N–90° N indicate a smaller decrease in emissions than priors (Figure S7) from 2000–2006 to 2007–2020. For SET1 and SET2, the posterior emissions indicate a larger increase in emissions from 2000–2006 to 2007–2020 compared to the priors at EQ–60° N. Global posterior coal emissions indicate a smaller increase in emissions from 2000–2006 to 2007–2020 compared to the priors, but there are differences between latitude bands. At latitudes of 30° N–60° N, the posterior trends are less than half of the priors in all simulations. At the latitudes 30° S–30° N, the posterior trend is similar to the priors over the time periods (Figures 3–5). At the latitudes 90° S–30° S and 60° N–90° N, the posterior trends differ from the priors, but the contribution is small (Table S3 and Figures S6 and S7). As a result, the global posterior coal emissions have a smaller magnitude compared to the priors expect for ORIG during 2000–2006 (Tables S2 and S3).

The global posterior CH_4 emission trends for rice are opposite to the priors, indicating a decrease in rice emissions (Figure 2). Estimated global residential emissions in ORIG increase less from 2000–2006 to 2007–2013 compared to priors, and there is decrease in the estimated emissions for 2014–2020 compared to 2000–2006 (Figure 2). The estimated global trends for fire emissions in ORIG are similar to the priors (Figure 2). The estimated global trends for wetland CH_4 emissions are decreasing in all simulations (Figure 2), although the magnitude of the emissions is 4.79 $TgCH_4$ yr^{-1} larger ($p < 0.05$) than the priors in SET1 (Table S3). Prior rice emissions have an increasing trend in all latitudinal bands, a small decreasing trend at 90° S–30° S and no trend at all at 60° N–90° N (Figures 3–5, S6 and S7). The decreasing trend for SET2 is the strongest among the simulations (Figure 2). The largest contribution to the differences between the prior and posterior comes from latitudes EQ–60° N (Figures 4 and 5). At latitudes 30° S–EQ, the posterior rice emission trends suggest a smaller increase in emissions compared to the priors (Figure 3). the estimated wetland CH_4 trends show some differences between the simulations at different latitude bands; e.g., the decreasing trend from 2000–2006 to 2014–2020 is stronger for SET1 than for ORIG at latitudes EQ–30° N but vice versa for 30° S–EQ (Figures 3 and 5).

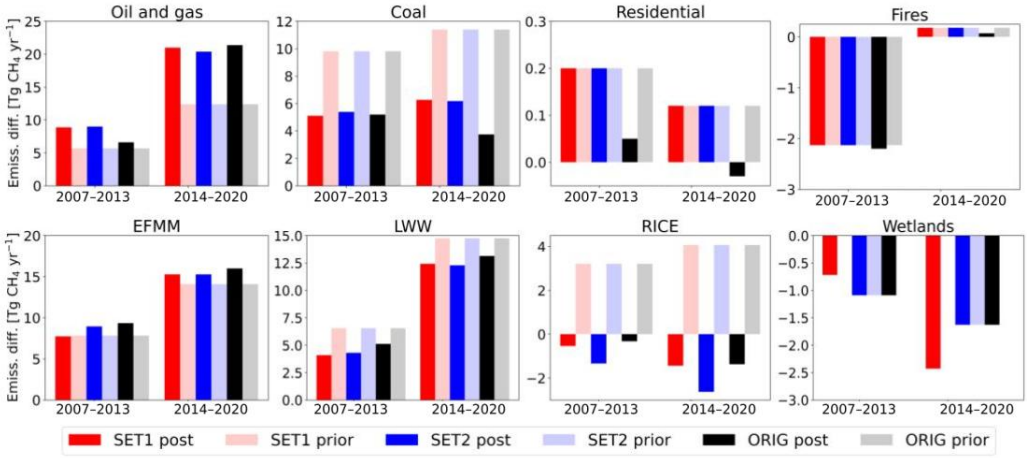

Figure 2. Difference in prior and posterior emissions globally from three different inversions compared to the years 2000–2006.

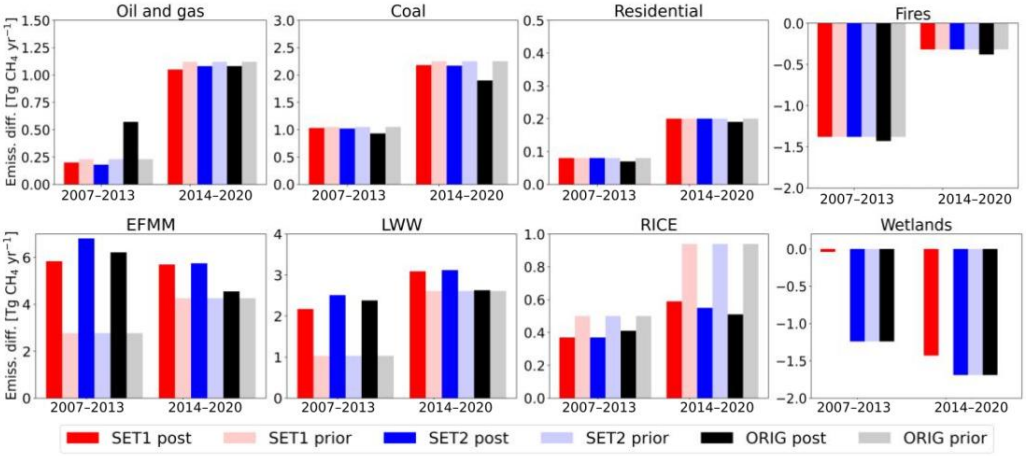

Figure 3. Difference in prior and posterior emissions at 30° S–EQ from three different inversions compared to the years 2000–2006.

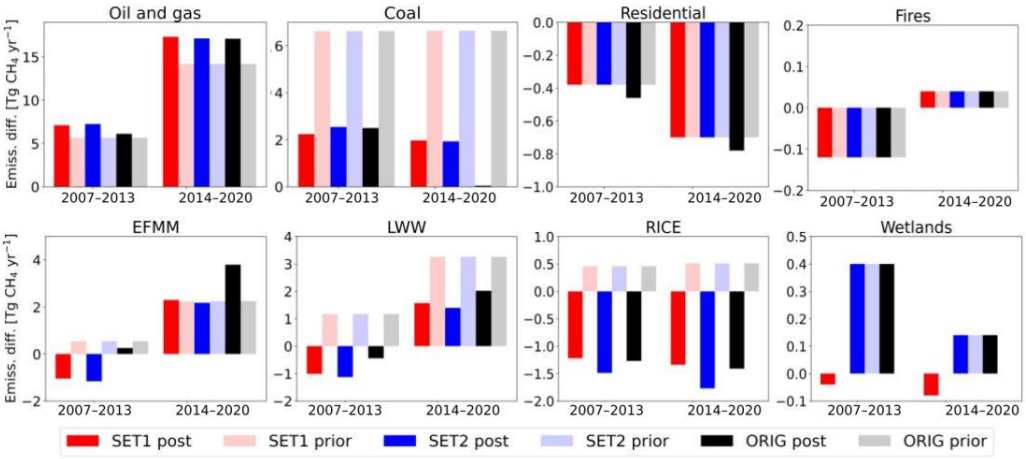

Figure 4. Difference in prior and posterior emissions at 30° N–60° N from three different inversions compared to the years 2000–2006.

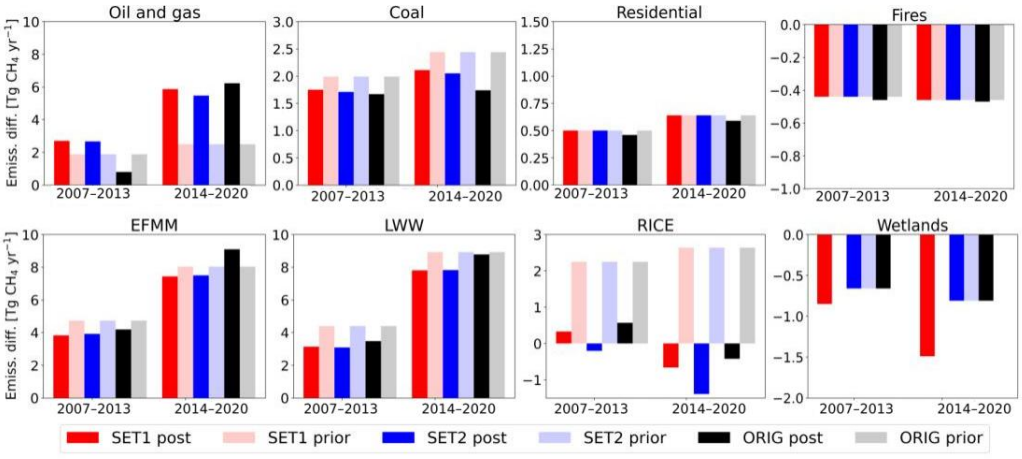

Figure 5. Difference in prior and posterior emissions at EQ–30° N from three different inversions compared to the years 2000–2006.

3.2. Estimated CH_4 and $\delta^{13}CH_4$ Trends

At almost all stations, the modeled CH_4 trends were in agreement with the observations, except for the WET simulation, which was not in agreement at any station. However,

there were large differences in the modeled $\delta^{13}CH_4$ trends between simulations but not between stations (Figures 6–9 and S8–S16). In general, the inversions were in better agreement with the observed $\delta^{13}CH_4$ trend from 2000 to 2012 than the priors; however, after 2012, all inversions showed no trend or an increasing trend, while the observations showed a decreasing trend. However, the COMBO_2 run with modified fossil and biogenic emissions agreed well with the observed $\delta^{13}CH_4$ trend. Here, we present a detailed analysis of the results for the four stations described in Section 2.3.2. The results from other stations are presented in the Supplementary Material (Figures S8–S16).

At BRW, anomalies for the modeled CH_4 differ from the observations (Figure 6). From 2012 to 2020, the modeled CH_4 trends in the anomalies are similar to the observations in all simulations except WET, but they start from a lower level. The simulated CH_4 anomalies in 2005 and 2010–2012 show a strong decrease, which is not seen in the observations. The modeled trends in $\delta^{13}CH_4$ show a similar behavior to that observed from 2000 to 2010, but the timing is different, so the modeled peaks and dips occur earlier.

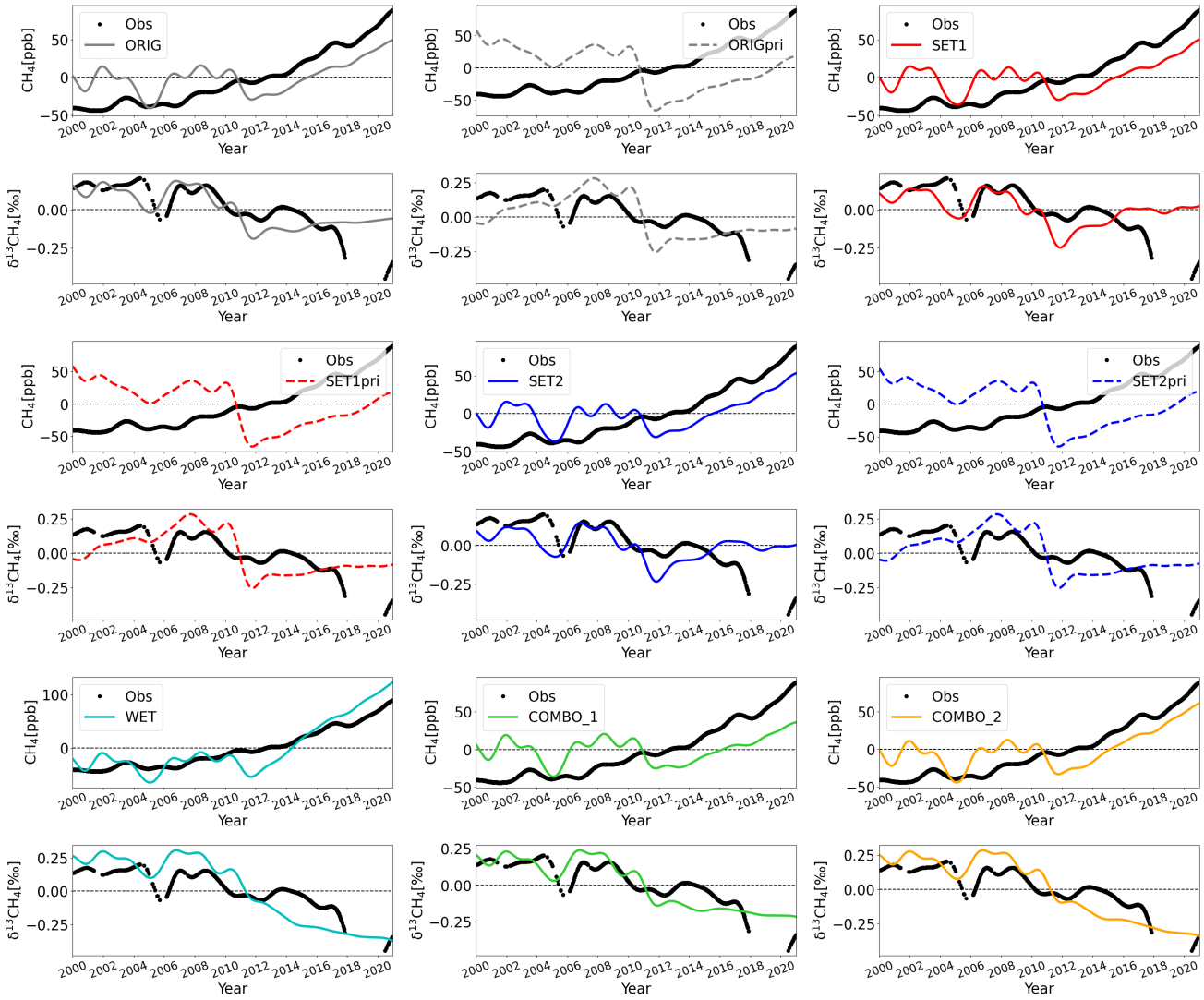

Figure 6. Anomalies in the CH_4 and $\delta^{13}CH_4$ trends at Barrow, Alaska, USA. Different simulations are shown with different colors. Simulations with prior emissions are shown as dashed lines. Note that ORIGpri and SET1pri are the same.

At MHD, the modeled and observed trends in the CH_4 anomaly are similar (Figure 7), except for WET. In addition, ORIG/SET1pri and SET2pri differ from observations before

2003. The modeled $\delta^{13}CH_4$ trends in WET and COMBO_2 are similar to the observations. The $\delta^{13}CH_4$ anomaly in the unmodified priors and posteriors shows increasing trends, despite the decreasing trend in the observations. The $\delta^{13}CH_4$ trend in COMBO_1 does not decrease as much as observations suggest after 2015.

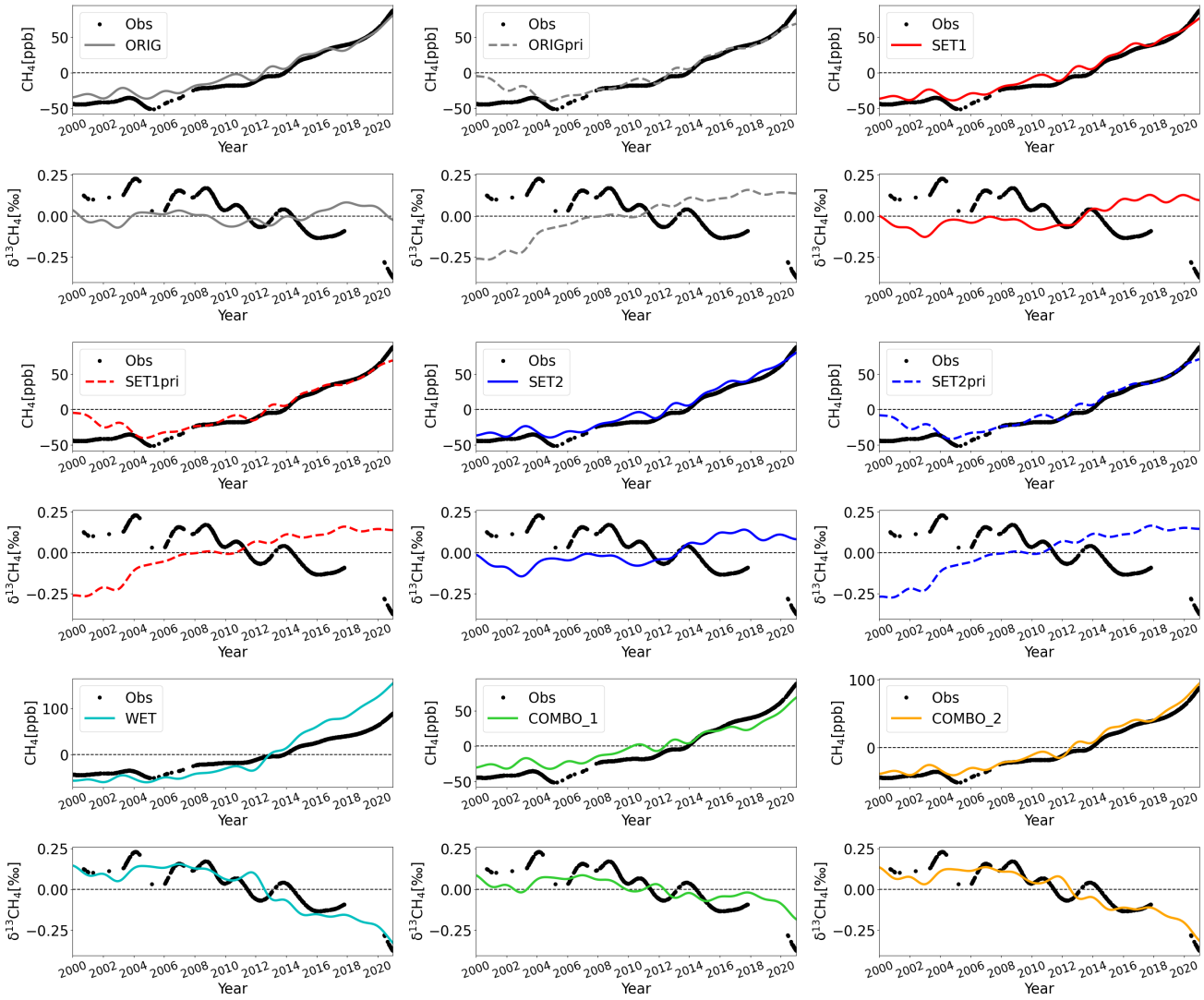

Figure 7. Anomalies in the CH_4 and $\delta^{13}CH_4$ trends at Mace Head, Ireland. Different simulations are shown with different colors. Simulations with prior emission are shown as dashed lines. Note that ORIGpri and SET1pri are the same.

At NWR, the modeled trends in the CH_4 anomaly are stronger in WET, but in other simulations, the trend agrees well with the observations, except for priors until 2002 (Figure 8). In contrast, the modeled $\delta^{13}CH_4$ trends in WET and COMBO_2 agree well with observations. The COMBO_1 simulation also has a similar trend to the observations, but the trend is weaker. Other simulations do not agree with the observations.

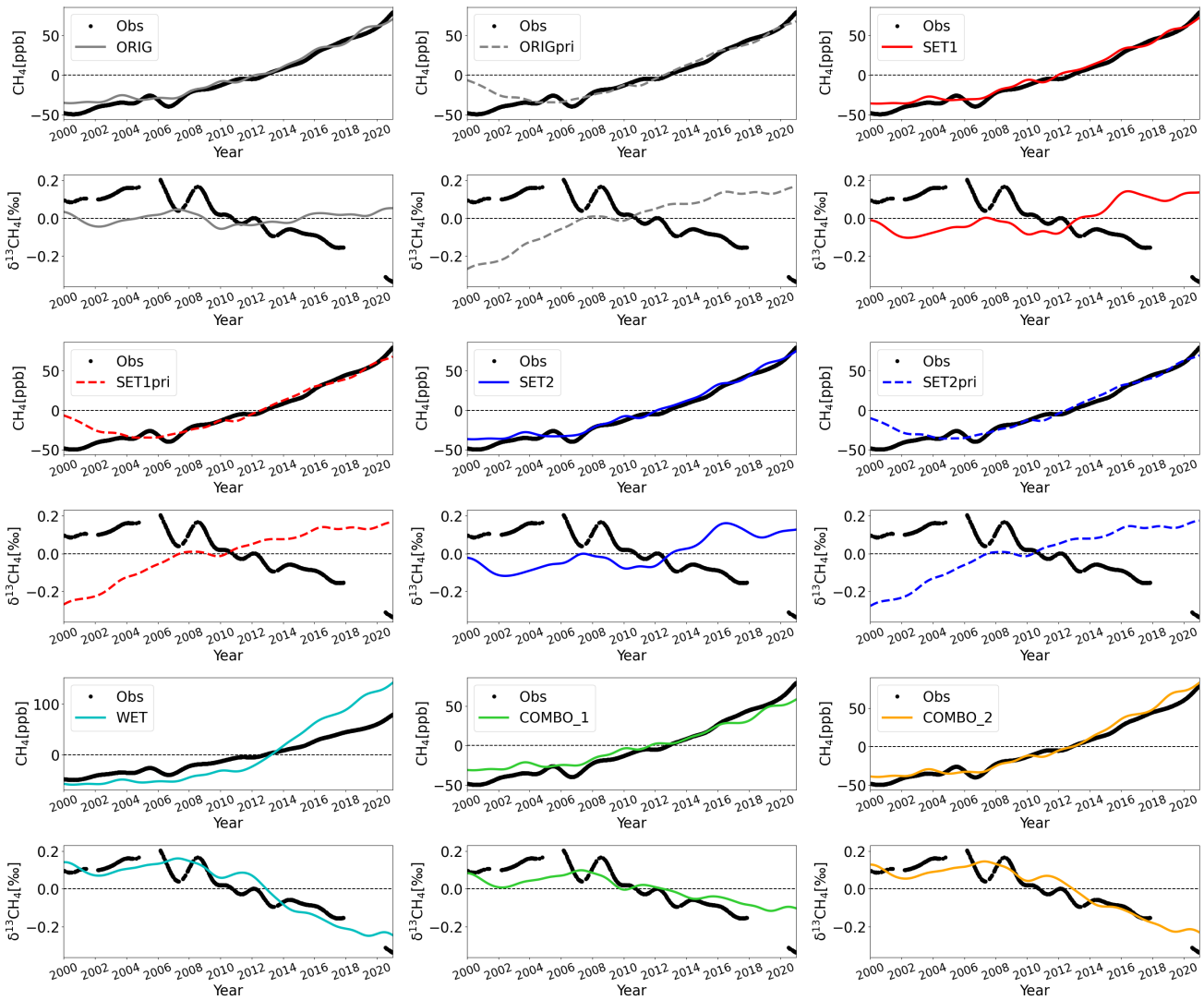

Figure 8. Anomalies in the CH_4 and $\delta^{13}CH_4$ trends at Niwot Ridge, Colorado, USA. Different simulations are shown with different colors. Simulations with prior emissions are shown as dashed lines. Note that ORIGpri and SET1pri are the same.

At SPO, the modeled and observed trends in the CH_4 anomaly are similar, except for WET. The priors are also different before 2003 (Figure 9). The observed trend in $\delta^{13}CH_4$ is similar to the observations in WET and COMBO_2 (Figure 9). The trend in COMBO_1 is decreasing but still weaker than the observations. Other simulations show an increasing trend in $\delta^{13}CH_4$, which is opposite to the observations.

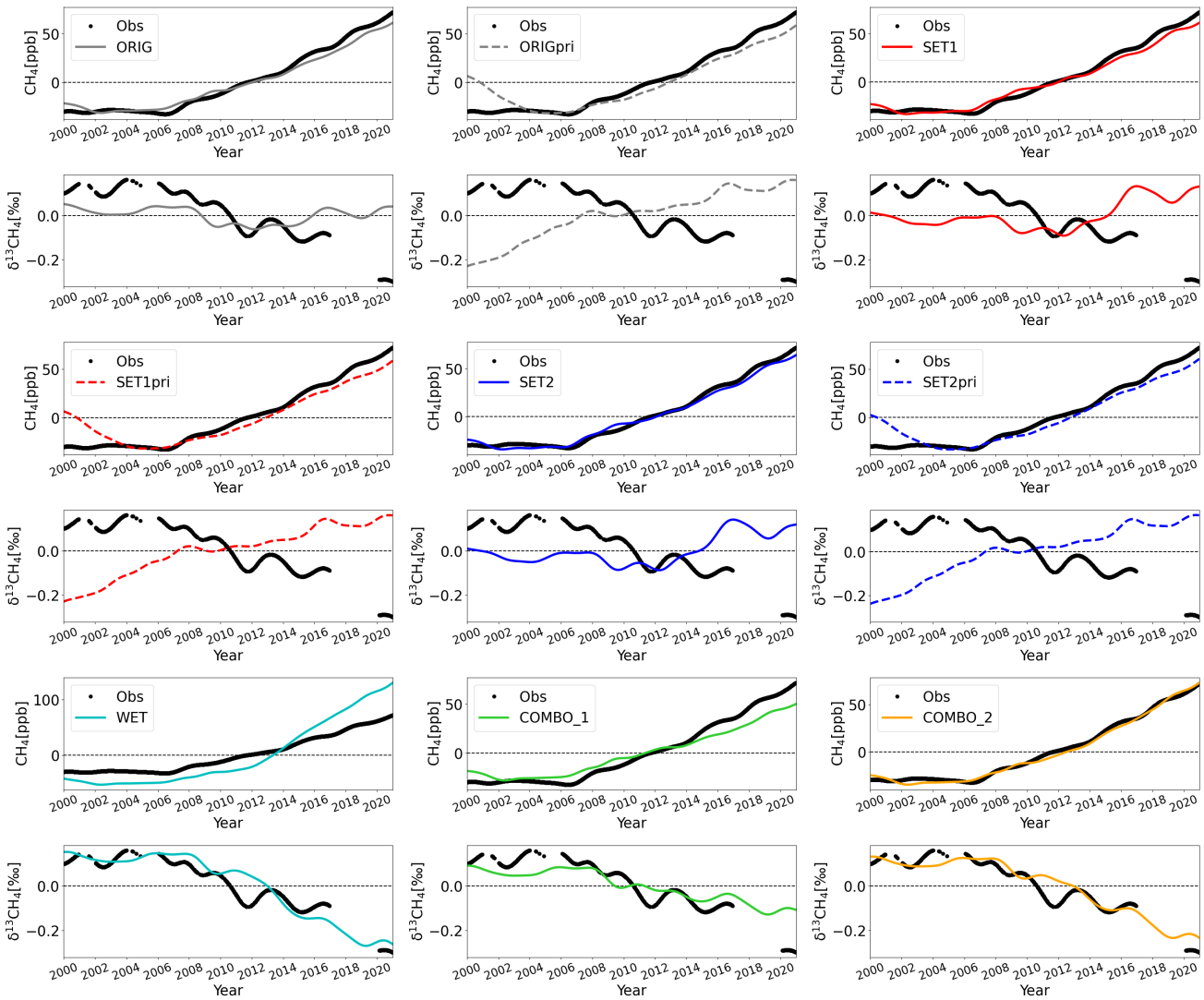

Figure 9. Anomalies in the CH_4 and $\delta^{13}CH_4$ trends at the South Pole, Antarctica. Different simulations are shown with different colors. Simulations with prior emissions are shown as dashed lines. Note that ORIGpri and SET1pri are the same.

4. Discussion

The TM5 results in this paper demonstrate the importance of initial emissions. We acknowledge that there are differences between emission inventories. Coal and oil and gas emissions in EDGARv6.0 differ from GAINS emissions in magnitude and trend in latitudinal bands. The total global emissions for coal and oil and gas in GAINS are 3.4 $TgCH_4$ yr^{-1} and 5.5 $TgCH_4$ yr^{-1} higher than in EDGAR v6.0, respectively. However, the global increasing trend for oil and gas from 2000–2006 to 2014–2020 is almost 50% smaller than for EDGAR v6.0. For coal, the increasing trend from 2000–2006 to 2007–2020 is similar to EDGAR v6.0. For example, at the latitudes EQ–30° N, the oil and gas emissions are 6.6 $TgCH_4$ yr^{-1} lower in GAINS, but coal emissions are 1.7 $TgCH_4$ yr^{-1} higher. Emissions from coal and oil and gas also vary between the EDGAR v6.0, v5.0 [48], and v4.3.2 [47].

The global trend of oil and gas emissions in GAINS according to our COMBO_2 results are consistent with the observed trends, as the results now suggest that oil and gas emissions are overestimated. However, the magnitude of oil and gas emissions in GAINS is larger compared to EDGAR v6.0 or the ORIG posterior. The global increasing trends in agricultural (including EFMM, LWW, and rice) and fossil (including coal and oil and gas) emissions are consistent with other bottom-up estimates by Stavert et al. [61], although

different prior emissions were used. However, the total magnitude of fossil emissions in bottom-up estimates is larger than the top-down estimates in Stavert et al. [61], but in this study, the estimated global fossil emissions are, on average, 0.8–1.43 $TgCH_4$ yr^{-1} smaller. The estimated agricultural emissions in this study are higher than prior emissions, contradicting the results of Stavert et al. [61].

Lan et al. [15] found that the increasing trend in EDGAR v4.3.2 anthropogenic fossil emissions did not match with the observed $\delta^{13}CH_4$ trend when simulated. Similarly, in this study, using EDGAR v6.0, the increasing CH_4 trend in anthropogenic fossil emissions did not match the observed $\delta^{13}CH_4$ trend in the simulation. The demonstration by Lan et al. [15] of changing partitioning of fossil and microbial emissions is consistent with our COMBO_2 scenario, where anthropogenic fossil emissions are reduced by 9% and anthropogenic biogenic emissions are increased by 8%. We also performed a TM5 simulation by increasing rice, LWW, and EFMM emissions, such that the biogenic and fossil ratio would increase by 2% (results not shown). However, such an increase would imply an increase of 18% (43.5 Tg yr^{-1}) in these emissions, which is outside the uncertainty range [1].

The inversions performed in this study were able to decrease the global coal emissions compared to priors throughout the years (on average 0.8–4.7 $TgCH_4$ yr^{-1}). However, the inversions were unable to decrease global oil and gas emissions, which were 5.88 $TgCH_4$ yr^{-1} higher than priors between 2014 and 2020. LWW and EFMM emissions were estimated to be larger tan priors, as suggested by the TM5 results. The inversions were unable to reduce fossil-based emissions enough, nor could they increase the agricultural emissions enough after 2012, but this can be explained by the inversion model's ability when the prior fluxes used are estimated wrongly, e.g., in magnitude or in spatial distribution. The TM5 results indicate that wetland CH_4 emissions should be optimized separately, as previously carried out by (e.g., [30,31]), and not together with agricultural emissions, as was carried out in this study. Furthermore, the TM5 results indicate that the contributions from biogenic sources to recent CH_4 trends need to be larger, which is consistent with Basu et al. [62]. In this study, we assimilated only CH_4 in the inversion, but there are studies that suggest it could be beneficial to simultaneously assimilate the $\delta^{13}CH_4$ and CH_4 [62].

We further acknowledge that temporal changes in isotopic signatures are important to consider when analyzing long-term trends. Seasonal variations have been reported for biogenic sources, such as wetlands [63,64] as well as rice cultivation [65–68]. Zazzeri et al. [69] reported that the coal source signatures vary depending on coal type, depth, coalification process, mining method, and coal rank. In addition, Liu et al. [70] reported that the $\delta^{13}CH_4$ signature changed in four stages during shale gas release. However, only limited data are available, and the signatures used in the study by Feinberg et al. [9] may be misreported.

We can assume that the time-invariant $\delta^{13}CH_4$ signatures used in this study are reasonable, since the modeled $\delta^{13}CH_4$ trend in the COMBO_2 simulation agrees with the observations. However, we cannot exclude the possibility that the time-invariant signatures could potentially lead to a misinterpretation of the modeled $\delta^{13}CH_4$ trend, as previously reported by Ganesan et al. [8] and Kangasaho et al. [44] in seasonal cycle analysis. There are limited studies on source-specific isotopic signatures changing over time (e.g., [71,72]). We did not consider isotopic signatures changing over time, but we acknowledge that this kind of variation may affect trends. We also acknowledge that including δ^2HCH_3 isotopes would provide additional information for source separation (e.g., [73]). However, there are not enough data available for δ^2HCH_3 isotopes to be used in this kind of modeling at present.

5. Conclusions

We performed global atmospheric inversions for CH_4 using CarbonTracker-Europe-CH_4 with different optimized emissions for 2000–2020. In addition, we performed a global atmospheric forward modeling analysis for CH_4 and $\delta^{13}CH_4$ using the inversion results to investigate which inversions corresponds best with observations.The results of the inversion simulations performed in this study suggest larger LWW and EFMM and lower

coal emissions than reported in EDGAR v6.0. This is supported by the results obtained with TM5 when analyzing the $\delta^{13}CH_4$ trends at different stations.

The results for TM5 indicate that the inversion obtained using EDGAR v6.0 emissions after 2012 is not able to reproduce the correct trend, in line with observations. The results of this study indicate that fossil-based emissions (coal, oil and gas, and residential) are overestimated by approximately 9% (approx. 12.31 Tg yr^{-1}), and biogenic emissions (rice, LWW, and EFMM) emissions are underestimated by approximately 8% (approx. 19.52 Tg yr^{-1}), after 2012 in the inversion using EDGAR v6.0. Interestingly, the modification of only CH_4 wetland emissions to produce a stronger decreasing $\delta^{13}CH_4$ trend, similar to observation results, in a CH_4 trend that is inconsistent with the observed CH_4 trend. This suggests that other emission sources, in addition to wetland emissions, should be modified despite the large uncertainty range of the wetland emissions. This study shows that the contribution of biogenic emissions needs to be larger after 2012 than what is in EDGAR v6.0. Furthermore, this study emphasizes the crucial role of the grouping of the optimized CH_4 emissions in atmospheric inversions to reproduce the observed $\delta^{13}CH_4$ trends from the CH_4 inversion results.

Despite the different optimized categories for CH_4 inversions, the modeled trend in TM5 for CH_4 did not differ much between simulations. However, there were differences in the modeled $\delta^{13}CH_4$ trends. When agricultural emissions are not included in the optimized biospheric CH_4 emissions, the modeled CH_4 and $\delta^{13}CH_4$ trends in TM5 agree better with the observations. Therefore, based on this study, it is recommended that CH_4 biospheric emissions are optimized with wetland emissions only, emission components are optimized individually, or, alternatively, the relationship between the emission components is traced to produce realistic trends for CH_4 and $\delta^{13}CH_4$. The results also show how sensitive the $\delta^{13}CH_4$ trend is to the correct CH_4 emissions, highlighting the importance of the CH_4 emissions used for simulations.

More research regarding $\delta^{13}CH_4$ signatures that possibly vary over time (periodically, seasonally or intermittently) would improve the understanding of the global CH_4 budget. In the future, more comprehensive research is needed on emissions inventories and how they match with the observed $\delta^{13}CH_4$ trend. As shown by this study, the emission inventories may be inconsistent with the observed $\delta^{13}CH_4$ trend, despite agreeing with the CH_4 trend. In the future, it would be worth investigating what additional information on source separation could be attained by simultaneously assimilating CH_4 and $\delta^{13}CH_4$ in inversion. In addition, it would be fruitful to investigate the reasons behind the observed trends of CH_4 and $\delta^{13}CH_4$ in more detail.

Supplementary Materials: The following supporting information can be downloaded at: https://www.mdpi.com/article/10.3390/atmos14071121/s1, Figure S1: 90° S–30° S prior and posterior CH_4 emissions by sector; Figure S2: 30° S–EQ prior and posterior CH_4 emissions by sector. Figure S3: EQ–30° N prior and posterior CH_4 emissions by sector; Figure S4: 30° N–60° N prior and posterior CH_4 emissions by sector; Figure S5: 60° N–90° N prior and posterior CH_4 emissions by sector; Figure S6: Difference in prior and posterior emissions at 90° S–30° S from three different inversions compared to years 2000–2006; Figure S7: Difference in prior and posterior emissions at 60° N–90° N from three different inversions compared to years 2000–2006; Figure S8: Anomalies in the CH_4 and $\delta^{13}CH_4$ trend at Alert, Canada; Figure S9: Anomalies in the CH_4 and $\delta^{13}CH_4$ trend at Terceira Island, Azores, Portugal; Figure S10: Anomalies in the CH_4 and $\delta^{13}CH_4$ trend at Tae-ahn Peninsula, Republic of Korea; Figure S11: Anomalies in the CH_4 and $\delta^{13}CH_4$ trend at Mt. Waliguan, Peoples Republic of China; Figure S12: Anomalies in the CH_4 and $\delta^{13}CH_4$ trend at Cape Kumukahi, Hawaii, United States; Figure S13: Anomalies in the CH_4 and $\delta^{13}CH_4$ trend at Mauna Loa, Hawaii, United States; Figure S14: Anomalies in the CH_4 and $\delta^{13}CH_4$ trend at Ascension Island, United Kingdom; Figure S15: Anomalies in the CH_4 and $\delta^{13}CH_4$ trend at Tutuila, American Samoa; Figure S16: Anomalies in the CH_4 and $\delta^{13}CH_4$ trend at Cape Grim, Tasmania, Australia; Table S1: List of stations; Table S2: Annual mean CH_4 emissions for 30° latitudinal bands during 2000–2020; Table S3: Posterior mean emissions for 30 degree latitudinal bands for different time periods.

Author Contributions: V.M., A.T. and T.A. designed the experiments. V.M. and A.T. developed the model code with help from L.B., S.H., A.S. and M.K. V.M. performed the simulations. V.M., A.T., L.B. and T.A. performed the analysis. X.L., E.J.D., S.M. and J.W.C.W. provided the observational data. M.S., B.P. and Z.Z. provided processed emissions inputs. V.M. prepared the manuscript with contributions from all co-authors. All authors have read and agreed to the published version of the manuscript.

Funding: We would like to thank Magnus Ehrnrooth Foundation, Academy of Finland (307331 UPFORMET), and EU-H2020 VERIFY. The VERIFY project has received funding from the European Union's Horizon 2020 research and innovation program under grant agreement No. 776810. Maarten Krol is supported by funding from the European Research Council (ERC) under the European Union's Horizon 2020 research and innovation program under grant agreement No. 742798.

Institutional Review Board Statement: Not applicable.

Informed Consent Statement: Not applicable.

Data Availability Statement: The atmospheric CH_4 and $\delta^{13}C$ measurements are available from the NOAA/GML data Server accessed on 1 April 2023 https://www.esrl.noaa.gov/gmd/dv/data/ (accessed on 22 April 2023).

Acknowledgments: We acknowledge obspack_ch4_1_GLOBALVIEWplus_v5.0_2022-10-17 providers fo their valuable work: Kenneth N. Schuldt, Tuula Aalto, Arlyn Andrews, Shuji Aoki, Francesco Apadula, Jgor Arduini, Bianca Baier, Jakub Bartyzel, Peter Bergamaschi, Tobias Biermann, Sebastien C. Biraud, Harald Boenisch, Gordon Brailsford, Willi A. Brand, Huilin Chen, Aurelie Colomb, Sébastien Conil, Cedric Couret, Paolo Cristofanelli, Emilio Cuevas, Bruce Daube, Kenneth Davis, Martine De Mazière, Marc Delmotte, Ankur Desai, Joshua P. DiGangi, Ed Dlugokencky, James W. Elkins, Lukas Emmenegger, Marc L. Fischer, Grant Forster, Luciana V. Gatti, Torsten Gehrlein, Christoph Gerbig, Emanuel Gloor, Daisuke Goto, László Haszpra, Juha Hatakka, Martin Heimann, Michal Heliasz, Daniela Heltai, Ove Hermanssen, Eric Hintsa, Antje Hoheisel, Jutta Holst, Viktor Ivakhov, Dan Jaffe, Armin Jordan, Warren Joubert, Hui-Yun Kang, Anna Karion, Victor Kazan, Ralph Keeling, Petri Keronen, Bert Kers, Jooil Kim, Tobias Kneuer, Mi-Young Ko, Katerina Kominkova, Eric Kort, Elena Kozlova, Paul Krummel, Dagmar Kubistin, Casper Labuschagne, Xin Lan, Ray Langenfelds, Olivier Laurent, Tuomas Laurila, Thomas Lauvaux, Jost Lavric, Choong-Hoon Lee, Haeyoung Lee, John Lee, Irene Lehner, Kari Lehtinen, Reimo Leppert, Ari Leskinen, Markus Leuenberger, Matthias Lindauer, Zoe Loh, Morgan Lopez, David Lowry, Chris R. Lunder, Toshinobu Machida, Ivan Mammarella, Giovanni Manca, Michal V. Marek, Melissa Y. Martin, Giordane A. Martins, Hidekazu Matsueda, Kathryn McKain, Frank Meinhardt, Malika Menoud, Natasha Miles, Charles E. Miller, John B. Miller, Vanessa Monteiro, Fred Moore, Heiko Moossen, Eric Morgan, Shinji Morimoto, David Munro, Cathrine L. Myhre, Meelis Mölder, Jenifer Müller-Williams, Jaroslaw Necki, Sylvia Nichol, Euan Nisbet, Yosuke Niwa, Simon O'Doherty, Florian Obersteiner, Salvatore Piacentino, Jean M. Pichon, Joseph Pitt, Jasna Pittman, Christian Plass-Duelmer, Stephen M. Platt, Maria E. Popa, Steve Prinzivalli, Michel Ramonet, Scott Richardson, Pedro P. Rivas, Michael Rothe, Thomas Röckmann, Kazuyuki Saito, Greg Santoni, Motoki Sasakawa, Bert Scheeren, Martina Schmidt, Tanja Schuck, Marcus Schumacher, Thomas Seifert, Mahesh K. Sha, Paul Shepson, Christopher D. Sloop, Paul Smith, Mila Stanisavljević, Martin Steinbacher, Britton Stephens, Colm Sweeney, Lise L. Sørensen, Kirk Thoning, Helder Timas, Margaret Torn, Pamela Trisolino, Jocelyn Turnbull, Kjetil Tørseth, Brian Viner, Gabriela Vitkova, Andrew Watson, Ray Weiss, Steve Wofsy, Justin Worsey, Doug Worthy, Sönke Zaehle, Andreas Zahn, Giulia Zazzeri, Rodrigo A. de Souza, Marcel de Vries, Alcide G. di Sarra, Carina van der Veen; Multi-laboratory compilation of atmospheric methane data for the period 1983–2021; obspack_ch4_1_GLOBALVIEWplus_v5.0_2022-10-17; NOAA Earth System Research Laboratory, Global Monitoring Laboratory. https://doi.org/10.25925/20221001. (Server accessed on 1 April 2023) We also acknowledge the Stable Isotopic Composition of Atmospheric Methane (13C) from the NOAA GML Carbon Cycle Cooperative Global Air Sampling Network, 1998–2021 (Michel, S.E., Clark, J.R., Vaughn, B.H., Crotwell, M., Madronich, M., Moglia, E., Neff, D., Mund, J. (2022), University of Colorado, Institute of Arctic and Alpine Research (INSTAAR). Stable Isotopic Composition of Atmospheric Methane (13C) from the NOAA GML Carbon Cycle Cooperative Global Air Sampling Network, 1998–2021. Version: 2022-12-15 https://doi.org/10.15138/9p89-1x02 (Server accessed on 1 April 2023).

Conflicts of Interest: The authors declare no conflicts of interest. The funders had no role in the design of the study; in the collection, analyses, or interpretation of data; in the writing of the manuscript; or in the decision to publish the results.

Abbreviations

The following abbreviations are used in this manuscript:

CTE-CHCH$_4$	CarbonTracker-Europe-CH$_4$
EnKF	Ensemble Kalman Filter
ECMWF	European Centre for Medium-Range Weather Forecasts
KIE	Kinetic isotopic effect
EDGAR	Emissions Database for Global Atmospheric Research
LWW	Landfills and waste water treatment
EFMM	Enteric Fermentation and Manure Managemnt
GFED	Global Fire Emissions Database
IPCC	Intergovernmental Panel on Climate Change
NOAA/GML	National Oceanic and Atmospheric Administration Global Monitoring Laboratory
INSTAAR	Institute of Arctic and Alpine Research
BRW	Barrow
MHD	Mace Head
NWR	Niwot Ridge
SPO	South Pole

References

1. Saunois, M.; Stavert, A.R.; Poulter, B.; Bousquet, P.; Canadell, J.G.; Jackson, R.B.; Raymond, P.A.; Dlugokencky, E.J.; Houweling, S.; Patra, P.K.; et al. The Global Methane Budget 2000–2017. *Earth Syst. Sci. Data* **2020**, *12*, 1561–1623. . [CrossRef]
2. Bergamaschi, P.; Karstens, U.; Manning, A.J.; Saunois, M.; Tsuruta, A.; Berchet, A.; Vermeulen, A.T.; Arnold, T.; Janssens-Maenhout, G.; Hammer, S.; et al. Inverse modelling of European CH_4 emissions during 2006–2012 using different inverse models and reassessed atmospheric observations. *Atmos. Chem. Phys.* **2018**, *18*, 901–920. [CrossRef]
3. Tsuruta, A.; Aalto, T.; Backman, L.; Krol, M.C.; Peters, W.; Lienert, S.; Joos, F.; Miller, P.A.; Zhang, W.; Laurila, T.; et al. Methane budget estimates in Finland from the CarbonTracker Europe-CH4 data assimilation system. *Tellus B Chem. Phys. Meteorol.* **2019**, *71*, 1565030. [CrossRef]
4. Dlugokencky, E.J.; Nisbet, E.G.; Fisher, R.; Lowry, D. Global atmospheric methane: Budget, changes and dangers. *Philos. Trans. R. Soc. A Math. Phys. Eng. Sci.* **2011**, *369*, 2058–2072. [CrossRef] [PubMed]
5. Nisbet, E.G.; Dlugokencky, E.J.; Manning, M.R.; Lowry, D.; Fisher, R.E.; France, J.L.; Michel, S.E.; Miller, J.B.; White, J.W.C.; Vaughn, B.; et al. Rising atmospheric methane: 2007–2014 growth and isotopic shift. *Glob. Biogeochem. Cycles* **2016**, *30*, 1356–1370. [CrossRef]
6. Sherwood, O.A.; Schwietzke, S.; Arling, V.A.; Etiope, G. Global Inventory of Gas Geochemistry Data from Fossil Fuel, Microbial and Burning Sources, version 2017. *Earth Syst. Sci. Data* **2017**, *9*, 639–656. [CrossRef]
7. Schwietzke, S.; Sherwood, O.A.; Bruhwiler, L.M.P.; Miller, J.B.; Etiope, G.; Dlugokencky, E.J.; Michel, S.E.; Arling, V.A.; Vaughn, B.H.; White, J.W.C.; et al. Upward revision of global fossil fuel methane emissions based on isotope database. *Nature* **2016**, *538*, 88–91. [CrossRef]
8. Ganesan, A.L.; Stell, A.C.; Gedney, N.; Comyn-Platt, E.; Hayman, G.; Rigby, M.; Poulter, B.; Hornibrook, E.R.C. Spatially Resolved Isotopic Source Signatures of Wetland Methane Emissions. *Geophys. Res. Lett.* **2018**, *45*, 3737–3745. [CrossRef]
9. Feinberg, A.I.; Coulon, A.; Stenke, A.; Schwietzke, S.; Peter, T. Isotopic source signatures: Impact of regional variability on the δ13CH4 trend and spatial distribution. *Atmos. Environ.* **2018**, *174*, 99–111. [CrossRef]
10. Etiope, G.; Ciotoli, G.; Schwietzke, S.; Schoell, M. Gridded maps of geological methane emissions and their isotopic signature. *Earth Syst. Sci. Data* **2019**, *11*, 1–22. [CrossRef]
11. Brownlow, R.; Lowry, D.; Fisher, R.E.; France, J.L.; Lanoisellé, M.; White, B.; Wooster, M.J.; Zhang, T.; Nisbet, E.G. Isotopic Ratios of Tropical Methane Emissions by Atmospheric Measurement: Tropical Methane δ ^{13} C Source Signatures. *Glob. Biogeochem. Cycles* **2017**, *31*, 1408–1419. [CrossRef]
12. Houweling, S.; Krol, M.; Bergamaschi, P.; Frankenberg, C.; Dlugokencky, E.J.; Morino, I.; Notholt, J.; Sherlock, V.; Wunch, D.; Beck, V.; et al. A multi-year methane inversion using SCIAMACHY, accounting for systematic errors using TCCON measurements. *Atmos. Chem. Phys.* **2014**, *14*, 3991–4012. [CrossRef]

13. Thompson, R.L.; Nisbet, E.G.; Pisso, I.; Stohl, A.; Blake, D.; Dlugokencky, E.J.; Helmig, D.; White, J.W.C. Variability in Atmospheric Methane from Fossil Fuel and Microbial Sources Over the Last Three Decades. *Geophys. Res. Lett.* **2018**, *45*, 11499–11508. [CrossRef]
14. Monteil, G.; Houweling, S.; Dlugockenky, E.J.; Maenhout, G.; Vaughn, B.H.; White, J.W.C.; Rockmann, T. Interpreting methane variations in the past two decades using measurements of CH_4 mixing ratio and isotopic composition. *Atmos. Chem. Phys.* **2011**, *11*, 9141–9153. [CrossRef]
15. Lan, X.; Basu, S.; Schwietzke, S.; Bruhwiler, L.M.P.; Dlugokencky, E.J.; Michel, S.E.; Sherwood, O.A.; Tans, P.P.; Thoning, K.; Etiope, G.; et al. Improved Constraints on Global Methane Emissions and Sinks Using δ13C-CH4. *Glob. Biogeochem. Cycles* **2021**, *35*, e2021GB007000. [CrossRef]
16. Saueressig, G.; Crowley, J.N.; Bergamaschi, P.; Brühl, C.; Brenninkmeijer, C.A.M.; Fischer, H. Carbon 13 and D kinetic isotope effects in the reactions of CH4 with O(1D) and OH: New laboratory measurements and their implications for the isotopic composition of stratospheric methane. *J. Geophys. Res. Atmos.* **2001**, *106*, 23127–23138. [CrossRef]
17. Cantrell, C.A.; Shetter, R.E.; McDaniel, A.H.; Calvert, J.G.; Davidson, J.A.; Lowe, D.C.; Tyler, S.C.; Cicerone, R.J.; Greenberg, J.P. Carbon kinetic isotope effect in the oxidation of methane by the hydroxyl radical. *J. Geophys. Res. Atmos.* **1990**, *95*, 22455–22462. [CrossRef]
18. Allan, W.; Struthers, H.; Lowe, D.C. Methane carbon isotope effects caused by atomic chlorine in the marine boundary layer: Global model results compared with Southern Hemisphere measurements. *J. Geophys. Res. Atmos.* **2007**, *112*, D04306. [CrossRef]
19. Hossaini, R.; Chipperfield, M.P.; Saiz-Lopez, A.; Fernandez, R.; Monks, S.; Feng, W.; Brauer, P.; Glasow, R.v. A global model of tropospheric chlorine chemistry: Organic versus inorganic sources and impact on methane oxidation. *J. Geophys. Res. Atmos.* **2016**, *121*, 14271–14297. [CrossRef]
20. Gromov, S.; Brenninkmeijer, C.A.M.; Jöckel, P. A very limited role of tropospheric chlorine as a sink of the greenhouse gas methane. *Atmos. Chem. Phys.* **2018**, *18*, 9831–9843. [CrossRef]
21. Lassey, K.; Ragnauth, S. Balancing the global methane budget: Constraints imposed by isotopes and anthropogenic emission inventories. *J. Integr. Environ. Sci.* **2010**, *7*, 97–107. [CrossRef]
22. Zhang, Y.; Jacob, D.J.; Lu, X.; Maasakkers, J.D.; Scarpelli, T.R.; Sheng, J.X.; Shen, L.; Qu, Z.; Sulprizio, M.P.; Chang, J.; et al. Attribution of the accelerating increase in atmospheric methane during 2010–2018 by inverse analysis of GOSAT observations. *Atmos. Chem. Phys.* **2021**, *21*, 3643–3666. [CrossRef]
23. Milkov, A.V.; Schwietzke, S.; Allen, G.; Sherwood, O.A.; Etiope, G. Using global isotopic data to constrain the role of shale gas production in recent increases in atmospheric methane. *Sci. Rep.* **2020**, *10*, 4199. [CrossRef]
24. Yin, Y.; Chevallier, F.; Ciais, P.; Bousquet, P.; Saunois, M.; Zheng, B.; Worden, J.; Bloom, A.A.; Parker, R.J.; Jacob, D.J.; et al. Accelerating methane growth rate from 2010 to 2017: Leading contributions from the tropics and East Asia. *Atmos. Chem. Phys.* **2021**, *21*, 12631–12647. [CrossRef]
25. Schaefer, H.; Fletcher, S.E.M.; Veidt, C.; Lassey, K.R.; Brailsford, G.W.; Bromley, T.M.; Dlugokencky, E.J.; Michel, S.E.; Miller, J.B.; Levin, I.; et al. A 21st-century shift from fossil-fuel to biogenic methane emissions indicated by 13CH4. *Science* **2016**, *352*, 80–84. [CrossRef] [PubMed]
26. Fujita, R.; Morimoto, S.; Maksyutov, S.; Kim, H.S.; Arshinov, M.; Brailsford, G.; Aoki, S.; Nakazawa, T. Global and Regional CH4 Emissions for 1995–2013 Derived From Atmospheric CH4, δ13C-CH4, and δD-CH4 Observations and a Chemical Transport Model. *J. Geophys. Res. Atmos.* **2020**, *125*, e2020JD032903. [CrossRef]
27. Zhang, Z.; Poulter, B.; Knox, S.; Stavert, A.; McNicol, G.; Fluet-Chouinard, E.; Feinberg, A.; Zhao, Y.; Bousquet, P.; Canadell, J.G.; et al. Anthropogenic emission is the main contributor to the rise of atmospheric methane during 1993–2017. *Natl. Sci. Rev.* **2021**, *9*, nwab200. [CrossRef]
28. Bousquet, P.; Ringeval, B.; Pison, I.; Dlugokencky, E.J.; Brunke, E.G.; Carouge, C.; Chevallier, F.; Fortems-Cheiney, A.; Frankenberg, C.; Hauglustaine, D.A.; et al. Source attribution of the changes in atmospheric methane for 2006–2008. *Atmos. Chem. Phys.* **2011**, *11*, 3689–3700. [CrossRef]
29. Dlugokencky, E.J.; Bruhwiler, L.; White, J.W.C.; Emmons, L.K.; Novelli, P.C.; Montzka, S.A.; Masarie, K.A.; Lang, P.M.; Crotwell, A.M.; Miller, J.B.; et al. Observational constraints on recent increases in the atmospheric CH4 burden. *Geophys. Res. Lett.* **2009**, *36 L18803* . [CrossRef]
30. Tsuruta, A.; Aalto, T.; Backman, L.; Hakkarainen, J.; Laan-Luijkx, I.T.v.d.; Krol, M.C.; Spahni, R.; Houweling, S.; Laine, M.; Dlugokencky, E.; et al. Global methane emission estimates for 2000–2012 from CarbonTracker Europe-CH_4 v1.0. *Geosci. Model Dev.* **2017**, *10*, 1261–1289. [CrossRef]
31. Bergamaschi, P.; Segers, A.; Brunner, D.; Haussaire, J.M.; Henne, S.; Ramonet, M.; Arnold, T.; Biermann, T.; Chen, H.; Conil, S.; et al. High-resolution inverse modelling of European CH_4 emissions using the novel FLEXPART-COSMO TM5 4DVAR inverse modelling system. *Atmos. Chem. Phys.* **2022**, *22*, 13243–13268. [CrossRef]
32. Peters, W.; Miller, J.B.; Whitaker, J.; Denning, A.S.; Hirsch, A.; Krol, M.C.; Zupanski, D.; Bruhwiler, L.; Tans, P.P. An ensemble data assimilation system to estimate CO_2 surface fluxes from atmospheric trace gas observations. *J. Geophys. Res. Atmos.* **2005**, *110 D24304* . [CrossRef]
33. Van der Laan-Luijkx, I.T.; van der Velde, I.R.; van der Veen, E.; Tsuruta, A.; Stanislawska, K.; Babenhauserheide, A.; Zhang, H.F.; Liu, Y.; He, W.; Chen, H.; et al. The CarbonTracker Data Assimilation Shell (CTDAS) v1.0: Implementation and global carbon balance 2001–2015. *Geosci. Model Dev.* **2017**, *10*, 2785–2800. [CrossRef]

34. Krol, M.; Houweling, S.; Bregman, B.; Broek, M.v.d.; Segers, A.; Velthoven, P.v.; Peters, W.; Dentener, F.; Bergamaschi, P. The two-way nested global chemistry-transport zoom model TM5: Algorithm and applications. *Atmos. Chem. Phys.* **2005**, *5*, 417–432. [CrossRef]
35. Tenkanen, M.; Tsuruta, A.; Rautiainen, K.; Kangasaho, V.; Ellul, R.; Aalto, T. Utilizing Earth Observations of Soil Freeze/Thaw Data and Atmospheric Concentrations to Estimate Cold Season Methane Emissions in the Northern High Latitudes. *Remote Sens.* **2021**, *13*, 5059. [CrossRef]
36. Spivakovsky, C.M.; Logan, J.A.; Montzka, S.A.; Balkanski, Y.J.; Foreman-Fowler, M.; Jones, D.B.A.; Horowitz, L.W.; Fusco, A.C.; Brenninkmeijer, C.a.M.; Prather, M.J.; et al. Three-dimensional climatological distribution of tropospheric OH: Update and evaluation. *J. Geophys. Res. Atmos.* **2000**, *105*, 8931–8980. [CrossRef]
37. Huijnen, V.; Williams, J.; van Weele, M.; van Noije, T.; Krol, M.; Dentener, F.; Segers, A.; Houweling, S.; Peters, W.; de Laat, J.; et al. The global chemistry transport model TM5: Description and evaluation of the tropospheric chemistry version 3.0. *Geosci. Model Dev.* **2010**, *3*, 445–473. [CrossRef]
38. Jöckel, P.; Tost, H.; Pozzer, A.; Brühl, C.; Buchholz, J.; Ganzeveld, L.; Hoor, P.; Kerkweg, A.; Lawrence, M.n.G. The atmospheric chemistry general circulation model ECHAM5/MESSy1: Consistent simulation of ozone from the surface to the mesosphere. *Atmos. Chem. Phys.* **2006**, *6*, 5067–5104. [CrossRef]
39. Zhao, Y.; Saunois, M.; Bousquet, P.; Lin, X.; Berchet, A.; Hegglin, M.I.; Canadell, J.G.; Jackson, R.B.; Hauglustaine, D.A.; Szopa, S.; et al. Inter-model comparison of global hydroxyl radical (OH) distributions and their impact on atmospheric methane over the 2000–2016 period. *Atmos. Chem. Phys.* **2019**, *19*, 13701–13723. [CrossRef]
40. Turner, A.J.; Frankenberg, C.; Kort, E.A. Interpreting contemporary trends in atmospheric methane. *Proc. Natl. Acad. Sci. USA* **2019**, *116*, 2805–2813. [CrossRef]
41. Rowlinson, M.J.; Rap, A.; Arnold, S.R.; Pope, R.J.; Chipperfield, M.P.; McNorton, J.; Forster, P.; Gordon, H.; Pringle, K.J.; Feng, W.; et al. Impact of El Niño–Southern Oscillation on the interannual variability of methane and tropospheric ozone. *Atmos. Chem. Phys.* **2019**, *19*, 8669–8686. [CrossRef]
42. Crowley, J.N.; Saueressig, G.; Bergamaschi, P.; Fischer, H.; Harris, G.W. Carbon kinetic isotope effect in the reaction CH4+Cl: A relative rate study using FTIR spectroscopy. *Chem. Phys. Lett.* **1999**, *303*, 268–274. [CrossRef]
43. Spahni, R.; Wania, R.; Neef, L.; van Weele, M.; Pison, I.; Bousquet, P.; Frankenberg, C.; Foster, P.N.; Joos, F.; Prentice, I.C.; et al. Constraining global methane emissions and uptake by ecosystems. *Biogeosciences* **2011**, *8*, 1643–1665. [CrossRef]
44. Kangasaho, V.; Tsuruta, A.; Backman, L.; Mäkinen, P.; Houweling, S.; Segers, A.; Krol, M.; Dlugokencky, E.J.; Michel, S.; White, J.W.C.; et al. The Role of Emission Sources and Atmospheric Sink in the Seasonal Cycle of CH4 and δ;13-CH4: Analysis Based on the Atmospheric Chemistry Transport Model TM5. *Atmosphere* **2022**, *13*, 888. [CrossRef]
45. Snover, A.K.; Quay, P.D. Hydrogen and carbon kinetic isotope effects during soil uptake of atmospheric methane. *Glob. Biogeochem. Cycles* **2000**, *14*, 25–39. [CrossRef]
46. De Laeter, J.R.; Böhlke, J.K.; Bièvre, P.D.; Hidaka, H.; Peiser, H.S.; Rosman, K.J.R.; Taylor, P.D.P. Atomic weights of the elements. Review 2000 (IUPAC Technical Report). *Pure Appl. Chem.* **2003**, *75*, 683–800. [CrossRef]
47. Janssens-Maenhout, G.; Crippa, M.; Guizzardi, D.; Muntean, M.; Schaaf, E.; Dentener, F.; Bergamaschi, P.; Pagliari, V.; Olivier, J.G.J.; Peters, J.A.H.W.; et al. EDGAR v4.3.2 Global Atlas of the three major greenhouse gas emissions for the period 1970–2012. *Earth Syst. Sci. Data* **2019**, *11*, 959–1002. [CrossRef]
48. Crippa, M.; Solazzo, E.; Huang, G.; Guizzardi, D.; Koffi, E.; Muntean, M.; Schieberle, C.; Friedrich, R.; Janssens-Maenhout, G. High resolution temporal profiles in the Emissions Database for Global Atmospheric Research. *Sci. Data* **2020**, *7*, 121. [CrossRef]
49. Giglio, L.; Randerson, J.T.; van der Werf, G.R. Analysis of daily, monthly, and annual burned area using the fourth-generation global fire emissions database (GFED4). *J. Geophys. Res. Biogeosci.* **2013**, *118*, 317–328. [CrossRef]
50. Weber, T.; Wiseman, N.A.; Kock, A. Global ocean methane emissions dominated by shallow coastal waters. *Nat. Commun.* **2019**, *10*, 4584. [CrossRef]
51. Contribution of Working Group I to the Sixth Assessment Report of the Intergovernmental Panel on Climate Change. In *Climate Change 2021: The Physical Science Basis*; Masson-Delmotte, V., Zhai, P., Pirani, A., Connors, S., Péan, C., Berger, S., Caud, N., Chen, Y., Goldfarb, L., Gomis, M., et al., Eds.; Cambridge University Press: Cambridge, UK; New York, NY, USA, 2021. [CrossRef]
52. Schuldt, K.N.; Aalto, T.; Andrews, A.; Aoki, S.; Apadula, F.; Arduini, J.; Baier, B.; Bartyzel, J.; Bergamaschi, P.; Biermann, T.; et al. *Multi-Laboratory Compilation of Atmospheric Carbon Dioxide Data for the Period 1957–2022*; Data Set; NOAA: Boulder, CO, USA, 2022. [CrossRef]
53. *Stable Isotopic Composition of Atmospheric Methane (13C) from the NOAA GML Carbon Cycle Cooperative Global Air Sampling Network, 1998–2021*; Version: 2022-12-15, University of Colorado, Institute of Arctic and Alpine Research (INSTAAR) Data Set; NOAA: Boulder, CO, USA, 2021. [CrossRef]
54. *Guidelines for the Measurement of Methane and Nitrous Oxide and their Quality Assurance*; WMO/TD-No. 1478, GAW Report No. 185; WMO: Geneva, Switzerland, 2009.
55. Miller, J.B.; Mack, K.A.; Dissly, R.; White, J.W.C.; Dlugokencky, E.J.; Tans, P.P. Development of analytical methods and measurements of 13C/12C in atmospheric CH4 from the NOAA Climate Monitoring and Diagnostics Laboratory Global Air Sampling Network. *J. Geophys. Res. Atmos.* **2002**, *107*, ACH 11-1–ACH 11-15. [CrossRef]

56. Bruhwiler, L.; Dlugokencky, E.; Masarie, K.; Ishizawa, M.; Andrews, A.; Miller, J.; Sweeney, C.; Tans, P.; Worthy, D. CarbonTracker-CH_4: An assimilation system for estimating emissions of atmospheric methane. *Atmos. Chem. Phys.* **2014**, *14*, 8269–8293. [CrossRef]
57. Thoning, K.W.; Tans, P.P.; Komhyr, W.D. Atmospheric carbon dioxide at Mauna Loa Observatory: 2. Analysis of the NOAA GMCC data, 1974–1985. *J. Geophys. Res. Atmos.* **1989**, *94*, 8549–8565. [CrossRef]
58. Still, C.J.; Berry, J.A.; Collatz, G.J.; DeFries, R.S. Global distribution of C3 and C4 vegetation: Carbon cycle implications. *Glob. Biogeochem. Cycles* **2003**, *17*, 6-1–6-14. [CrossRef]
59. Sherwood, O.; Schwietzke, S.; Arling, V.; Etiope, G. Global Inventory of Fossil and Non-fossilMethane δ^{13}C Source Signature Measurements for Improved Atmospheric Modeling. Available online: https://gml.noaa.gov/ccgg/arc/index.php?id=134 (accessed on 1 April 2023).
60. Bakkaloglu, S.; Lowry, D.; Fisher, R.E.; Menoud, M.; Lanoisellé, M.; Chen, H.; Röckmann, T.; Nisbet, E.G. Stable isotopic signatures of methane from waste sources through atmospheric measurements. *Atmos. Environ.* **2022**, *276*, 119021. [CrossRef]
61. Stavert, A.R.; Saunois, M.; Canadell, J.G.; Poulter, B.; Jackson, R.B.; Regnier, P.; Lauerwald, R.; Raymond, P.A.; Allen, G.H.; Patra, P.K.; et al. Regional trends and drivers of the global methane budget. *Glob. Chang. Biol.* **2022**, *28*, 182–200. [CrossRef]
62. Basu, S.; Lan, X.; Dlugokencky, E.; Michel, S.; Schwietzke, S.; Miller, J.B.; Bruhwiler, L.; Oh, Y.; Tans, P.P.; Apadula, F.; et al. Estimating emissions of methane consistent with atmospheric measurements of methane and δ^{13}C of methane. *Atmos. Chem. Phys.* **2022**, *22*, 15351–15377. [CrossRef]
63. Fisher, R.E.; France, J.L.; Lowry, D.; Lanoisellé, M.; Brownlow, R.; Pyle, J.A.; Cain, M.; Warwick, N.; Skiba, U.M.; Drewer, J.; et al. Measurement of the 13C isotopic signature of methane emissions from northern European wetlands. *Glob. Biogeochem. Cycles* **2017**, *31*, 605–623. [CrossRef]
64. Sriskantharajah, S.; Fisher, R.E.; Lowry, D.; Aalto, T.; Hatakka, J.; Aurela, M.; Laurila, T.; Lohila, A.; Kuitunen, E.; Nisbet, E.G. Stable carbon isotope signatures of methane from a Finnish subarctic wetland. *Tellus B Chem. Phys. Meteorol.* **2012**, *64*, 18818. [CrossRef]
65. Tyler, S.C.; Brailsford, G.W.; Yagi, K.; Minami, K.; Cicerone, R.J. Seasonal variations in methane flux and δl3CH4 values for rice paddies in Japan and their implications. *Glob. Biogeochem. Cycles* **1994**, *8*, 1–12. [CrossRef]
66. Bergamaschi, P. Seasonal variations of stable hydrogen and carbon isotope ratios in methane from a Chinese rice paddy. *J. Geophys. Res. Atmos.* **1997**, *102*, 25383–25393. [CrossRef]
67. Zhang, G.; Ma, J.; Yang, Y.; Yu, H.; Shi, Y.; Xu, H. Variations of Stable Carbon Isotopes of CH4 Emission from Three Typical Rice Fields in China. *Pedosphere* **2017**, *27*, 52–64. [CrossRef]
68. Marik, T.; Fischer, H.; Conen, F.; Smith, K. Seasonal variations in stable carbon and hydrogen isotope ratios in methane from rice fields. *Glob. Biogeochem. Cycles* **2002**, *16*, 41-1–41-11. [CrossRef]
69. Zazzeri, G.; Lowry, D.; Fisher, R.E.; France, J.L.; Lanoisellé, M.; Kelly, B.F.J.; Necki, J.M.; Iverach, C.P.; Ginty, E.; Zimnoch, M.; et al. Carbon isotopic signature of coal-derived methane emissions to the atmosphere: From coalification to alteration. *Atmos. Chem. Phys.* **2016**, *16*, 13669–13680. [CrossRef]
70. Liu, Y.; Liang, F.; Shang, F.; Wang, Y.; Zhang, Q.; Shen, Z.; Su, C. Carbon isotope fractionation during shale gas release: Experimental results and molecular modeling of mechanisms. *Gas Sci. Eng.* **2023**, *113*, 204962. [CrossRef]
71. Chang, J.; Peng, S.; Ciais, P.; Saunois, M.; Dangal, S.R.S.; Herrero, M.; Havlík, P.; Tian, H.; Bousquet, P. Revisiting enteric methane emissions from domestic ruminants and their δ 13 C CH4 source signature. *Nat. Commun.* **2019**, *10*, 3420. [CrossRef]
72. Oh, Y.; Zhuang, Q.; Welp, L.R.; Liu, L.; Lan, X.; Basu, S.; Dlugokencky, E.J.; Bruhwiler, L.; Miller, J.B.; Michel, S.E.; et al. Improved global wetland carbon isotopic signatures support post-2006 microbial methane emission increase. *Commun. Earth Environ.* **2022**, *3*, 159. [CrossRef]
73. Takriti, M.; Ward, S.E.; Wynn, P.M.; McNamara, N.P. Isotopic characterisation and mobile detection of methane emissions in a heterogeneous UK landscape. *Atmos. Environ.* **2023**, *305*, 119774. [CrossRef]